iScience

CellPress
OPEN ACCESS

Article

SART1 modulates poly-(ADP-ribose) chain accumulation and PARP1 chromatin localization

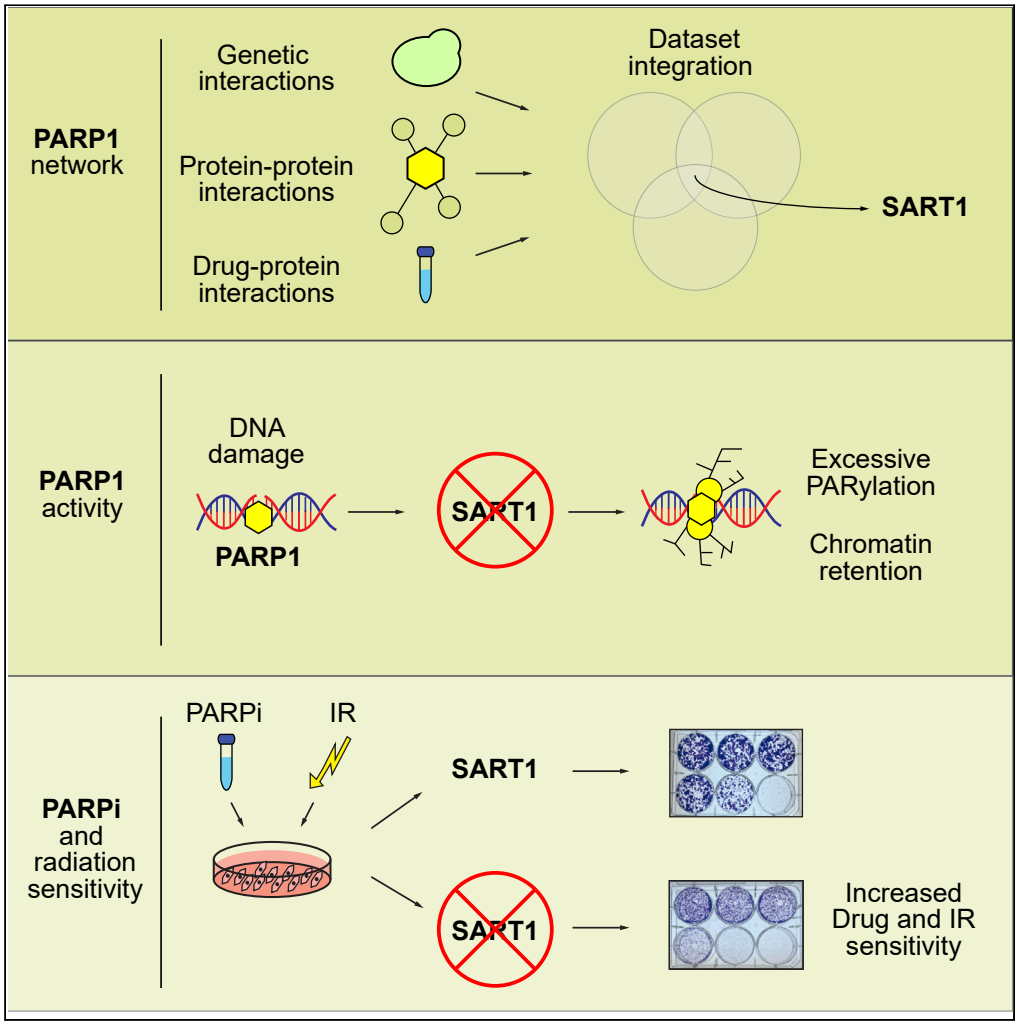

Samuele Lodovichi, Thales C. Nepomuceno, Nicholas T. Woods, ..., Achille Pellicioli, Alvaro Galli, Alvaro N.A. Monteiro

87samuele@gmail.com (S.L.)
alvaro.monteiro@moffitt.org (A.N.A.M.)

Highlights

SART1 was identified as a candidate modulator of PARP1 function

SART1 silencing leads to an increase in poly-ADP ribosylation

Accumulation of PAR chains is dependent on the SART1 RGG/RG motif

SART1 silencing increases sensitivity to PARP inhibitors and to ionizing radiation

Lodovichi et al., iScience 27, 111252
November 15, 2024
https://doi.org/10.1016/j.isci.2024.111252

iScience

CellPress
OPEN ACCESS

Article

SART1 modulates poly-(ADP-ribose) chain accumulation and PARP1 chromatin localization

Samuele Lodovichi,[1,2,6,*] Thales C. Nepomuceno,[1] Nicholas T. Woods,[3] Uwe Rix,[4] John M. Koomen,[5] Achille Pellicioli,[6] Alvaro Galli,[2] and Alvaro N.A. Monteiro[1,7,*]

SUMMARY

PARP1 inhibitors (PARPis) are used for treatment of cancers with mutations in *BRCA1* or *BRCA2* that are deficient in homologous recombination. The identification of modulators of PARP1 activity is critical to understand and overcome resistance to PARPis. We integrated data from three omics-scale screens to discover new regulators of PARP1 activity. We identified SART1 and show that its silencing leads to an increase in poly-ADP ribosylation and chromatin-bound PARP1. SART1 is recruited to chromatin following DNA damage and limits PARP1 chromatin retention and activity. The SART1 N-terminus is sufficient to regulate the accumulation of PAR chains and PARP1 on chromatin, an activity dependent on the RGG/RG box. Silencing of SART1 leads to an increased sensitivity of cells to DNA damage induced by IR, irrespective of *BRCA1* status and to PARPis only in absence of *BRCA1*. These results suggest that SART1 could be clinically utilized to improve PARPi efficacy.

INTRODUCTION

The poly(ADP-ribose) polymerase 1 (PARP1) gene encodes a nuclear protein that transfers ADP-ribose residues from the oxidized form of nicotinamide adenine dinucleotide (NAD^+) onto target substrates.[1] Poly(ADP-ribosyl)ation (PARylation) reactions are widely used in eukaryotes and only a small number of eukaryotic species lack the *PARP1* gene.[2]

PARP1 is able to both PARylate target proteins, including itself, and to regulate a wide variety of cellular processes such as DNA repair, chromatin remodeling, DNA replication, RNA metabolism, and cell cycle control.[1,3–5] Several amino acid residues, such as Lys, Arg, Glu, Asp, Cys, Ser, Thr, His, and Tyr can be a target of PARylation and interaction with cofactors can switch preference for specific residues.[6–8] PARP1 is involved in repair of single and double strand DNA breaks (SSB and DSB) by acting as a docking platform through the generation of long ADP-ribose chains and regulating several downstream factors involved in the DNA damage response (DDR).[9]

Recognition of exposed bases at DNA damage sites by PARP1 induces conformational changes, which lead to NAD^+ binding and allows the activation of its PARylation activity.[10] A variety of amino acid residues can act as acceptors of PARylation.[11–13] During DNA damage repair, histone PARylation factor 1 (HPF1) is recruited to DNA damage sites in a PARP1-dependent manner, modifying PARP1 target specificity to favor serine residues.[14] PAR chains are recognized by diverse proteins through several PAR-binding modules, such as the BRCT (BRCA1 C-terminal), PBZ (PAR-binding zinc finger), the OB-fold and the PIN (PilT N-terminus) domains.[15] More recently, PAR-reading motifs enriched in arginine and glycine residues, named RGG/RG boxes, have been identified in RNA-binding proteins mediating their recruitment to DNA damage sites.[16]

Inhibition of PARP1 is now widely used in cancer therapy to treat cancers where DNA repair, particularly through homologous recombination (HR), is defective, such as ovarian, breast, prostate, and pancreatic cancers caused by inactivation of *BRCA1* or *BRCA2*.[17] In addition, PARP1 inhibitors (PARPis) may provide a benefit even in the absence of inactivating mutations in *BRCA1/2*, likely due to epigenetic inactivation or to pathogenic variants in other DNA repair-related genes.[18] Recently, a limiting role of PARP1 on BRCA1 activity has been shown where PARylation of BRCA1 is essential to avoid excessive DSBs resection, which could also explain PARPi sensitivity in *BRCA1*-proficient cells.[19]

To date, four PARPis have been approved by the Food and Drug Administration (FDA): olaparib, rucaparib, niraparib, and talazoparib, which act as NAD^+ mimetic binding to PARP1 catalytic site.[20,21] However, the underlying molecular mechanism of action by which PARPis induce their anti-cancer activities is still incompletely understood. Currently, proposed modes of action involve inhibition of SSB repair

[1]Department of Cancer Epidemiology, H. Lee Moffitt Cancer Center and Research Institute, Tampa, FL 33612, USA
[2]Yeast Genetics and Genomics, Laboratory of Functional Genetics and Genomics, Institute of Clinical Physiology, CNR, 56125 Pisa, Italy
[3]Gastrointestinal Cancer Program, Eppley Institute for Research in Cancer, Fred & Pamela Buffett Cancer Center, University of Nebraska Medical Center, Omaha, NE 68198, USA
[4]Department of Drug Discovery, H. Lee Moffitt Cancer Center and Research Institute, Tampa, FL 33612, USA
[5]Molecular Oncology and Molecular Medicine Program, H. Lee Moffitt Cancer Center, Tampa, FL 33612, USA
[6]Dipartimento di Bioscienze, Università degli Studi di Milano, 20131 Milano, Italy
[7]Lead contact
*Correspondence: 87samuele@gmail.com (S.L.), alvaro.monteiro@moffitt.org (A.N.A.M.)
https://doi.org/10.1016/j.isci.2024.111252

and trapping of PARP1 protein on chromatin leading to the collapse of replication forks. Both actions lead to a common outcome: the accumulation of lethal DSB in the absence of *BRCA1* or *BRCA2*.[22]

Despite their demonstrated clinical efficacy, primary, and acquired resistance are current limitations.[23–26] Although several mechanisms of resistance have been described including reversion of inactivating mutations in *BRCA1* and *BRCA2*, epistatic mutations in *TP53BP1* and *REV7*, and upregulation of multidrug efflux transporters, a significant portion of these cases are not explained by known mechanisms.[20,27] Moreover, *BRCA* status has been shown to be an imperfect predictor of PARPi response and there is a need for additional mechanism-based biomarkers and targets to enhance efficacy of PARPis to be used in combinatorial approaches.[28]

Here, we integrate results from two previous omics-scale independent genetic and biochemical experimental datasets to identify modulators of PARP1 activity[29,30] with a new PARP1 BRCT-protein interaction network generated by tandem affinity purification coupled to mass spectrometry. We then focus on the role of the top candidate in our approach, spliceosome associated factor 1 (SART1), in modulating PARP1 activity. *SART1* was initially identified as a gene coding for two distinct proteins which contain tumor rejection epitopes capable of inducing cytotoxic T lymphocytes in cancer patients.[31] Both SART1 proteins, a nuclear 800 aa and a cytosolic 259 aa protein were later found to be required for the assembly of mature spliceosomes as components of the U4/U6-U5 tri-snRNP.[32] SART1 (800 aa), the subject of our study, was also found to be implicated in 5-fluorouracil and SN38 drug resistance in colorectal cancer.[33]

RESULTS

Identification of PARP1 BRCT interactors

To identify candidate protein-protein interactions relevant for the DDR we focused on the BRCT domain, a self-folding modular domain found in 26 human proteins critical to cellular signaling in the cellular response to DNA damage.[34,35] Purification of the BRCT domain from human PARP1 (aa 375–486) and its interacting proteins was obtained by tandem affinity purification followed by mass spectrometry (TAP-MS), as previously described.[34] TAP-tagged green fluorescent protein (GFP) served as a negative control. All affinity purifications used lysates from 293FT cells collected 2 h after exposure to 20 Gy ionizing radiation (IR) to enrich for post-translational modifications induced by DNA damage such as phosphorylation and PARylation. A total of 271 high confidence PARP1 BRCT interacting proteins were identified in the PARP1 BRCT TAP-MS experiments (Figure 1A) (Table S1).

Identification of modulators of PARP1 inhibitor sensitivity

To identify interactors more likely to be novel modulators of PARPi sensitivity, we searched for targets present in two additional omics-scale datasets relevant for PARP1 activity. The second dataset (n = 88) contains proteins coded by human homologs of yeast genes that display a genetic interaction with PARP1 (Figure 1A) (Table S2).[29] It contains a set of genes whose deletion is required for rescuing the small colony phenotype resulting from ectopic expression of a human PARP1 cDNA,[36] and therefore required for PARP1 function. The third dataset contains human proteins (n = 118) that biochemically interact with talazoparib directly or indirectly by engaging the PARPi/PARP1/2 complexes *in cellulo*.[30] We posited that genes/proteins present in more than one dataset would increase the likelihood to identify a significant contributor to PARPi sensitivity. Only one protein, SART1, was present in all three datasets (Figure 1B) (Table S2). SART1 (also known as SNUT1) has been previously implicated in RNA splicing as a component of the spliceosome.[32]

Expression of SART1 mRNA across normal human tissues

To inform the choice of cancer models in which to explore the role of SART1 in PARPi sensitivity, we first examined the levels of expression of *SART1* mRNA across normal human tissues (GTEx; https://www.gtexportal.org/home/). Interestingly, tissues of the female reproductive tract (uterus, endocervix, ectocervix, ovary, and fallopian tube) have the highest expression levels of *SART1* mRNA across all normal tissues. Ovarian and fallopian tube tissue display the highest level of *SART1* mRNA expression among the tissues of origin of tumors linked to inactivation of *BRCA1/2* (i.e., breast, ovarian, prostate, and pancreatic cancer) as shown in Figure S1A.

Alterations in SART1 across human cancers

Next, we probed for SART1 somatic alterations in cancer samples through cBioPortal (https://www.cbioportal.org/) focusing our attention on cancers where PARPis were used as a therapy. We queried the portal selecting samples from ovarian serous cystadenocarcinoma (TCGA, Firehose Legacy), breast invasive carcinoma (TCGA, PanCancer Atlas), pancreatic adenocarcinoma (TCGA, Firehose Legacy), prostate adenocarcinoma (TCGA, Firehose Legacy) where copy number alteration and mutation data are available. Ovarian samples (fallopian tube has a small sample size) display the highest rate of *SART1* alteration (10%) and the highest rate of amplification among all the tissues analyzed (Figures S1A and S1B), leading to higher *SART1* mRNA levels (Figures S1A–S1D). These data prompted us to explore the role of SART1 in PARP1 activity and PARPi sensitivity in ovarian cancer cells.

SART1 localization and binding to PARP1 are modulated by DNA damage

Our TAP-MS screen for interactors of the PARP1 BRCT domains suggested that SART1 and PARP1 interacted in a BRCT-mediated manner. Notably, the interaction between the endogenous SART1 and PARP1 proteins is detectable only in the presence of IR-induced DNA damage (Figure 2A). Next, we investigated the extent to which SART1 sub-cellular localization is influenced by DNA damage. The ratio between SART1

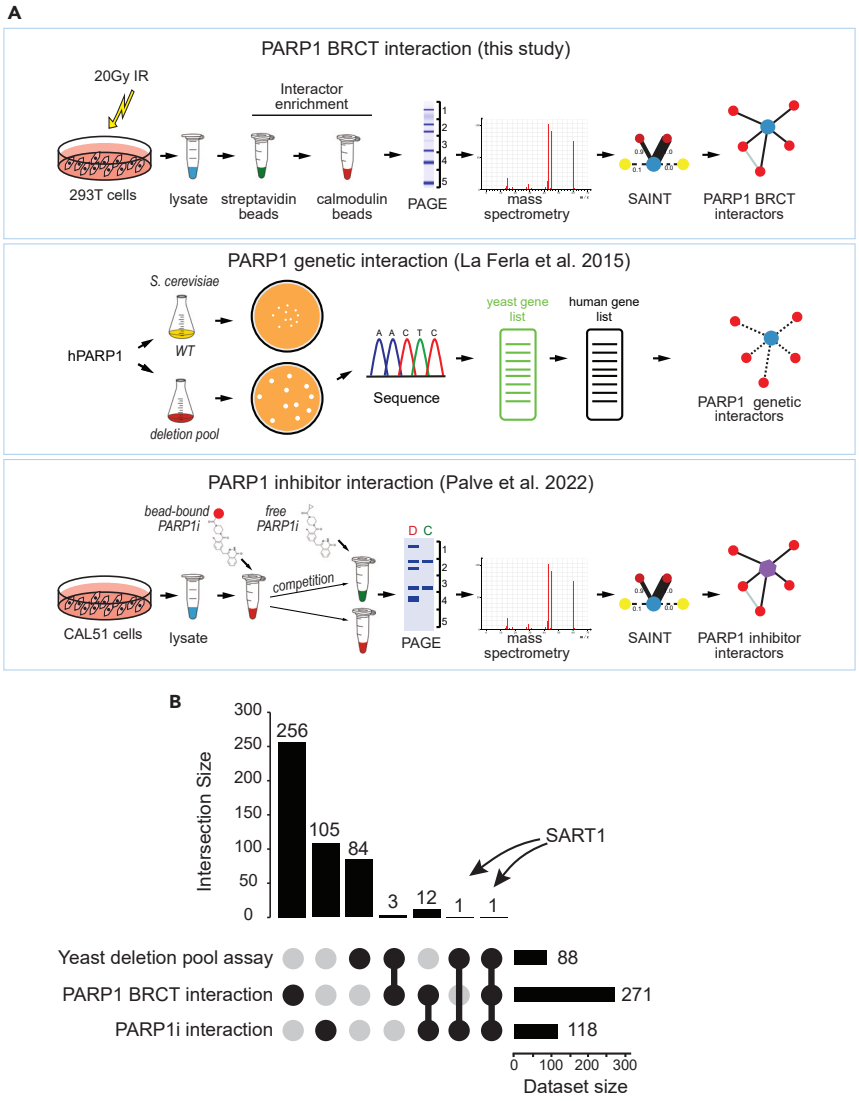

Figure 1. Assays intersection results and data from publicly available databases

(A) Study design and approaches to obtain each dataset. IR, ionizing radiation, PAGE, polyacrylamide gel electrophoresis; PARP1i, PARP1 inhibitors; SAINT, Significance Analysis of INTeractome.

(B) UpSet plot showing number of targets identified in each assay analyzed in this study and their intersections. Vertical bars represent the size of the intersection. The three leftmost bars represent the number of elements in each set that does not intersect with the other datasets. The other bars represent the intersection between datasets indicated in the matrix below the graph. Horizontal bars indicate the size of each dataset.

nuclear and cytoplasmic signal is increased 1 h after IR treatment. Staining cells for Cyclin B1 to determine whether nuclear localization could be a function of cell cycle showed that the IR-induced nuclear localization is independent of cell cycle phase (Figure 2B).

SART1 silencing leads to lower PARP1 protein levels

To assess the role of SART1 in ovarian cancer cells we generated UWB1.289 (UWB) ovarian cancer cell line stably silenced for *SART1*, combining two shRNAs targeting the coding and non-coding sequences. UWB1.289 cells are null for *BRCA1*. We obtained a reduction to less than 30% of the original protein expression (Figure 3A). Interestingly, silencing of SART1 also led to a reduction in PARP1 levels (Figures 3A and 3B). This effect is reproducible in other cell types, suggesting it is a general phenomenon (Figure S2).

SART1 silencing increases PARylation pre and post IR treatment

To assess SART1's role in DNA damage-induced PARylation, *SART1*-proficient or -deficient (silenced for *SART1*) cells were treated with 4 Gy of IR and cellular PARylation was analyzed before IR, 4 and 8 h after irradiation. In cells proficient for *SART1*, SART1, and PARP1 protein levels

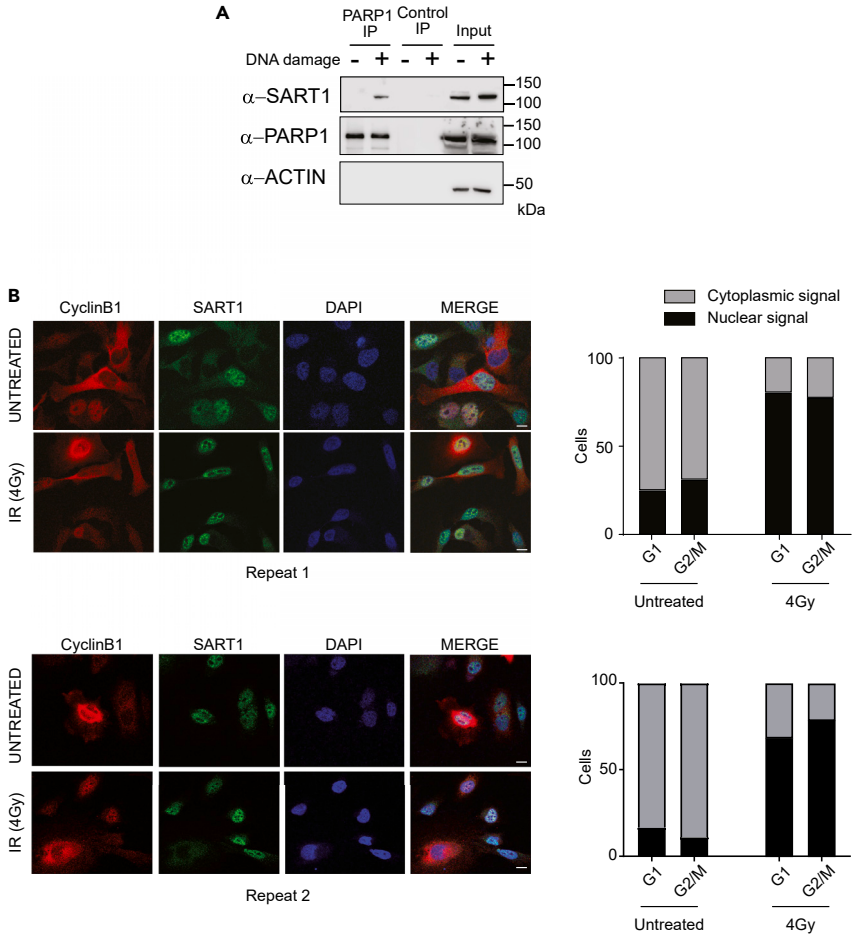

Figure 2. SART1 interaction with PARP1 and cellular localization are modified by DNA damage

(A) SART1-PARP1 interaction is induced by DNA damage as measured by immunoprecipitation in the presence or absence of DNA damage (6 Gy IR).

(B) Immunofluorescence analysis of HeLa cells untreated or treated with 4 Gy of IR. Cells were fixed on coverslips 4 h after treatment and blotted with anti-SART1 antibody, DAPI staining was performed to visualize the nuclei of cells. DAPI and SART1 signal were merged to discriminate cytoplasmic and nuclear localization of SART1. One hundred cells were counted and assessed for nuclear or cytoplasmic SART1 signal. Results of the counts are shown as histograms on the right part of the figure. Scale bar, 1 μm. Two independent experiments are shown (Repeat 1 and 2).

increase in tandem at 4 h after IR treatment induction, and after 8 h returns to a pre-IR level (Figure 3C). Interestingly, *SART1*-deficient cells have higher levels of PARylation when compared with *SART1*-proficient cells in the absence or in the presence of DNA damage, even with lower PARP1 levels (Figure 3C), suggesting that SART1 is required for the control of PARP1 PARylation activity.

SART1 silencing influences PARP1 chromatin localization pre and post IR treatment

Next, we fractionated nuclear lysates into nucleoplasm and chromatin fractions at the same time points after DNA damage induction as described previously. In SART1-proficient cells, PARP1 decreases in the nucleoplasm and has the highest chromatin localization at 4 h after DNA damage induction and it returns to a level comparable to the untreated sample after 8 h (Figures 3D and 3E). Upon DNA damage induction, SART1 levels increase in the nucleoplasm and in the chromatin fraction. Chromatin-associated SART1 levels are the highest level at the 8-h time point, concomitant with the decrease of chromatin-associated PARP1 (Figure 3E). On the other hand, chromatin-bound PARP1 in untreated *SART1*-deficient cells was higher than in *SART1*-proficient cells, and treatment with IR led to a reduction in chromatin-associated PARP1 associated with its accumulation in the nucleoplasm (Figures 3D and 3E). These data show that SART1 modulates PARP1 chromatin association.

Distinct protein domains control SART1 chromatin localization

Since SART1 is detected in the chromatin concomitant with increases in both PARylation and the chromatin-bound PARP1 (Figures 3C and 3D), we hypothesized that SART1 was being recruited to the chromatin via an RG/RGG-rich motif, which recognizes PAR polymers.[37] Multiple sequence alignment of SART1 revealed two conserved RG/RGG-rich motifs, one close to the N-terminal (aa 59 to 69) with three

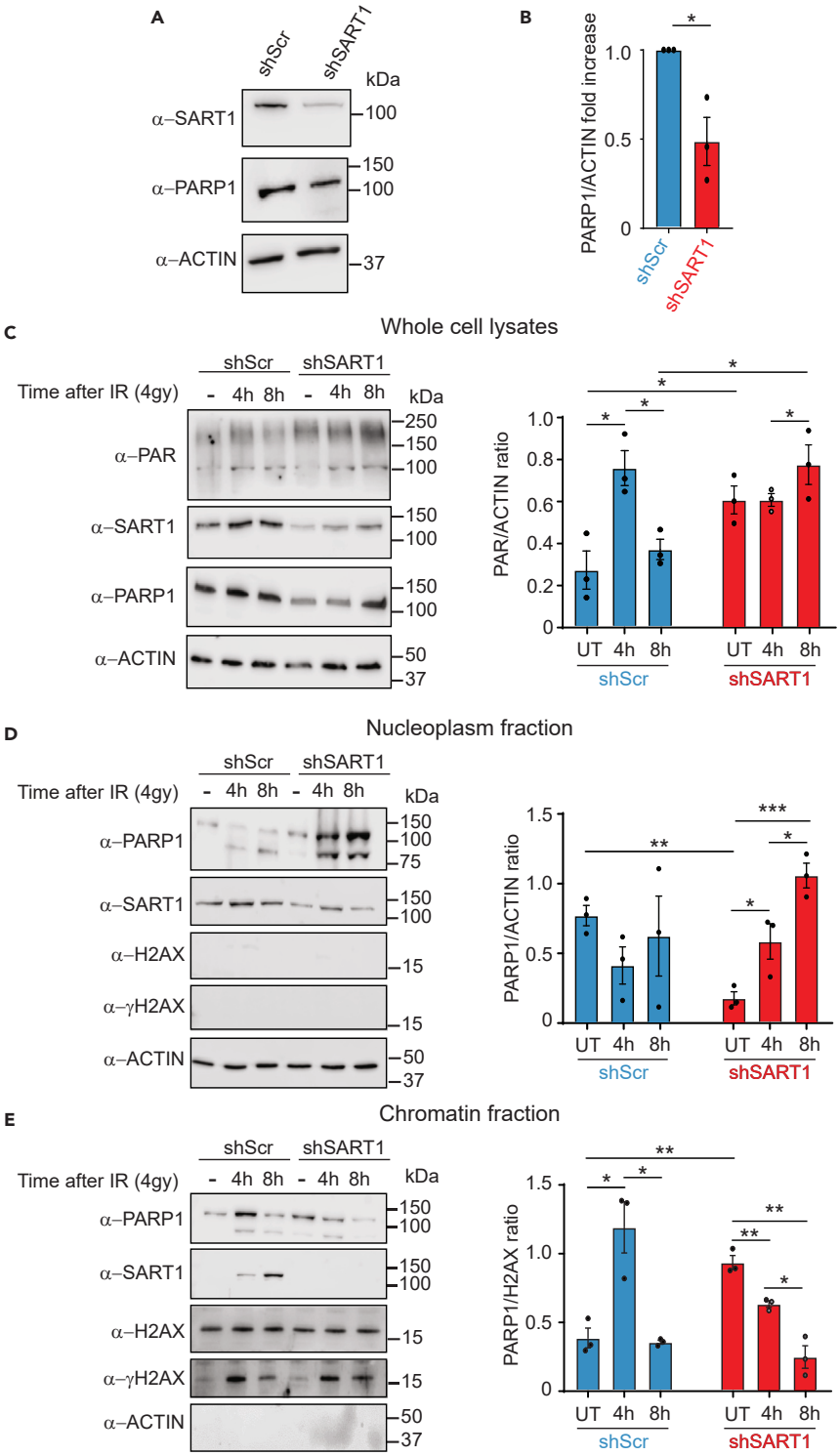

Figure 3. Silencing of *SART1*

(A) Blot showing efficiency of *SART1* silencing and effect on PARP1 protein level. UWB cells were transduced with two *SART1* shRNAs and silencing and PARP1 levels were assessed by western blot.

(B) Fold change in PARP1 levels is represented as mean ± SE of three independent experiments.

Figure 3. *Continued*

(C–E) PARylation levels in presence or absence of SART1 with and without DNA damage induction are shown in whole cell lysates (C), nucleoplasm (D), and chromatin (E) fractions. UWB cells proficient or silenced for *SART1* were mock treated or treated with 4 Gy of IR and collected at 4 h and 8 h after treatment. PAR levels have been evaluated using an anti-PAR antibody and their intensity has been measured using ImageJ software. An anti-γ-H2AX antibody has been used to monitor DNA damage. Data are shown as mean ± SE of three independent experiments and analyzed with Student's t test. *$p < 0.05$, **$p < 0.01$, ***$p < 0.001$.

repeats (RGG/RG/RG) and the second in the central part of the protein (aa 438 to 446) with two repeats (RG/RG) (Figure 4A). Furthermore, the SART1 N-terminal region is predicted (1% FP rate) to contain an intrinsically disordered region encompassing the first 125 amino acid residues (Figure S3). The C-terminal part of SART1 contains a cluster of serine residues (S667, S738, S787, S789, and S792) which could be the target of PARylation by PARP1.[8,12,38] Based on these features, we divided SART1 in three fragments (Figure 4A): fragment 1 (F1) from residue 1 to 250, fragment 2 (F2) from residue 235 to 490 and fragment 3 (F3) from residue 480 to 800. All fragments were expressed in *SART1*-silenced cell lines using only the shRNA targeting the 3'UTR of the sequence (Figure 4A).

While all three fragments are detectable in the cytoplasmic and nucleoplasmic fraction, only F1 and to a lesser extent F3, localize to chromatin (Figures 4B and 4C). Interestingly, F1 association to chromatin is DNA damage independent, whereas F3 chromatin localization is increased upon DNA damage (Figure 4C). Cells expressing fragments that localize to chromatin (F1 and F3) have a pattern of chromatin-bound PARP1 similar to the one observed in *SART1*-proficient cells, suggesting that they can restore, at least in part, SART1 regulation of PARP1 chromatin association (Figure 4C). Conversely, cells expressing F2, which is unable to localize to chromatin, do not show a DNA damage-induced PARP1 chromatin association (Figure 4C).

Interestingly, while F2 weakly interacts with PARP1 in a DNA damage-independent fashion, F1 and particularly F3 shows increased PARP1 binding after DNA damage induction (Figure 4D). Notably, no interaction was detected between F1 and PARP1 in untreated cells, suggesting that F1 chromatin association does not require interaction with PARP1.

The SART1 N-terminal RG/RGG-rich motif suppresses the accumulation of PAR polymers

To further explore the relationship between different domains of SART1 and PARylation, we transfected cells stably silenced for endogenous *SART1* and reconstituted with either SART1 fragments or the full-length SART1, as control we transfected both the silenced and the *SART1*-proficient cell lines with the empty plasmid. The day after transfection, cells were treated with IR and samples were collected before irradiation, and 4 h and 8 h after irradiation and PAR polymers formation was assessed (Figure 5A). Expression of SART1 fragments or the full-length SART1 did not change PARP1 levels nor PARP1 cellular localization (Figure S4).

SART1-proficient and -deficient cells transfected with the empty vector recapitulate the results observed in Figure 3C (left panel). Overexpression of full length SART1 results in a marked reduction of PAR polymer accumulation (Figure 5B), consistent with the data showing that SART1 silencing increases PAR polymer formation.

Interestingly, expression of F1, which localizes to chromatin independently of DNA damage, leads to a reduction in PAR accumulation comparable to that obtained by the ectopic expression of the full-length protein in the presence or absence of DNA damage (Figure 5B; lanes 1–3, right panel and lanes 3–5, left panel). Expression of F2, which fails to localize to chromatin, does not change the pattern of PAR accumulation in mock-treated or IR-treated *SART1*-deficient cells (Figure 5B; lanes 4–6, right panel and lanes 7–9, left panel). Expression of F3, which localizes to chromatin only after DNA damage induction, leads to a different pattern of PAR accumulation. Baseline (mock-treated cells) PAR levels are relatively low and progressively increase after treatment with DNA damage reaching the highest level in the series at 8 h after IR (Figure 5B; lanes 7–9, right panel).

To determine the role of the RG/RGG-rich motif in the ability of F1 to localize to chromatin and to regulate PARylation, we mutated the $R^{59}GG$ motif to $A^{59}AA$ (F1-ALA) (Figure 5C). The mutated F1 fails to suppress the accumulation of PAR polymers, but it is still able to localize to chromatin. Disruption of this motif leads to its progressive accumulation in chromatin after DNA damage (Figures 5D and 5E).

These data indicate that the N-terminal RG/RGG-rich motif containing R^{59} is required for the SART1-mediated control of PAR polymer accumulation and its chromatin retention.

SART1 silencing sensitizes cells to PARPis and to DNA damage while reducing RAD51 and increasing RIF1 recruitment to DNA damage sites

Next, we assessed the role of *SART1* in sensitivity of ovarian cancer cells to PARP1 inhibitors and DNA damage caused by IR. We compared the *SART1-deficient* (UWB shSART1) with *SART1*-proficient (UWB control shRNA) cells. Silencing *SART1* significantly increased sensitivity to rucaparib, talazoparib, or DNA damage caused by IR (Figures 6A and S6A).

Interestingly, while silencing *SART1* in *BRCA1*-reconstituted cells (UWB+B) did not modulate sensitivity to olaparib, rucaparib, or talazoparib, it increased sensitivity to IR (Figures 6B and S6B). Analysis in an additional ovarian cancer cell line (HEY A8) proficient for *BRCA1* generated comparable results, showing a slight increase in sensitivity to olaparib and talazoparib treatment when SART1 is downregulated (Figure S5A).

Next, to address the feasibility of a combination treatment, we combined IR to PARPi treatment to see if this would enhance sensitivity to the latter. Combination with IR makes the difference between *SART1*-deficient and -proficient more pronounced in cells treated with olaparib, rucaparib, or talazoparib, suggesting that a combination treatment with PARPi and DNA damaging agents could be feasible (Figures 6 and S5).

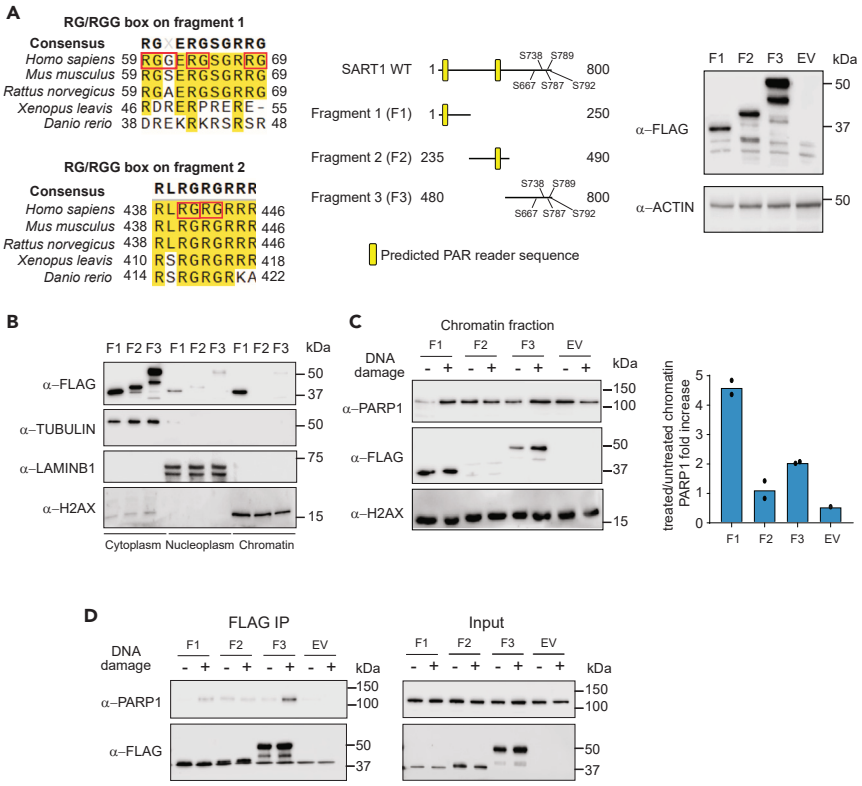

Figure 4. SART1 fragment cellular localization, influence on PARP1 chromatin binding and PARP1 interaction

(A) SART1 sequence analysis and fragment design. Left panel, multiple sequence analysis (ClustalW). Residues in yellow are conserved and red boxes indicate RG/RGG-rich motifs. Central panel, schema of the full length SART1 (WT), the three fragments created, the location of RG/RGG-rich motifs, and the cluster PARylated serine residues (F3). Right panel, western blot showing expression of each fragment in 293T cells.

(B) SART1 fragments' cellular localization. UWB cells were transfected with vectors expressing SART1 F1, F2, F3 or empty plasmid. Tubulin, lamin-B1, and histone H2AX have been used as cytoplasm, nuclear, and chromatin references, respectively.

(C) Chromatin fraction in UWB cells after expression of SART1 fragments and then untreated or treated with 4 Gy of IR. UWB cells were transfected with vector expressing SART1 F1, F2, F3 or empty plasmid, the day after cells were mock-treated or irradiated with 4 Gy of IR and collected after 4 h. Change in PARP1 chromatin level between treated and untreated sample was measured with ImageJ and normalized on chromatin loading control.

(D) SART1 fragments-PARP1 interaction in presence or absence of DNA damage. 293T cells were transfected with plasmids expressing SART1 fragments or empty vector and cells collected untreated or 4 h after 8 Gy irradiation.

Finally, to investigate the molecular underpinnings underlying the increase in PARPi sensitivity, we indirectly analyzed the efficiency of DNA repair using the recruitment of RAD51 and RIF1 to bleomycin-induced nuclear foci, as proxies for HR and NHEJ repair, respectively (Figure 7A). RAD51 and RIF1 focus formation was assessed in *SART1*-proficient and -deficient G2/M cells (Cyclin-B1-positive). In the presence of DNA damage, *SART1* silencing led to a reduction in RAD51 foci formation with a concomitant increase in RIF1 signal (Figures 7B and 7C). These results, using recruitment of RAD51 and RIF1 as proxies for HR and NHEJ repair, respectively, suggest SART1 downregulation shifts the choice of repair from an error-free to an error-prone pathway.

DISCUSSION

The identification of targets that can modulate PARP1 activity is critical to understand the mechanisms of action of PARPis and to circumvent resistance. Previous work has identified targets implicated in the DDR such as ataxia telangiectasia and rad3-related kinase (ATR), ataxia telangiectasia mutated kinase (ATM), DNA dependent protein kinase (DNA-PK), and the wee-like kinase 1 (WEE1).[39–44] Small molecule inhibitors of these proteins are already in early phase clinical development and the efficacy of their combination with PARPis is currently under study.[45,46]

Here, we build on previous work and identify spliceosome associated factor 1 (SART1), a component of the U4/U6-U5 tri-snRNP, as a modulator of PARP1 function and PARPi sensitivity. Other RNA-binding proteins have been shown to be recruited to DNA damage sites via binding to PAR chains.[47–49] Recently, another component of spliceosomal complex has been shown to localize to DNA lesions in a PAR-dependent manner.[50]

Our data are consistent with a model in which SART1, progressively recruited to chromatin following DNA damage, limits PARP1 chromatin retention and activity at late stages of DNA repair preventing the formation of cytotoxic PARP1-DNA complexes. Interestingly,

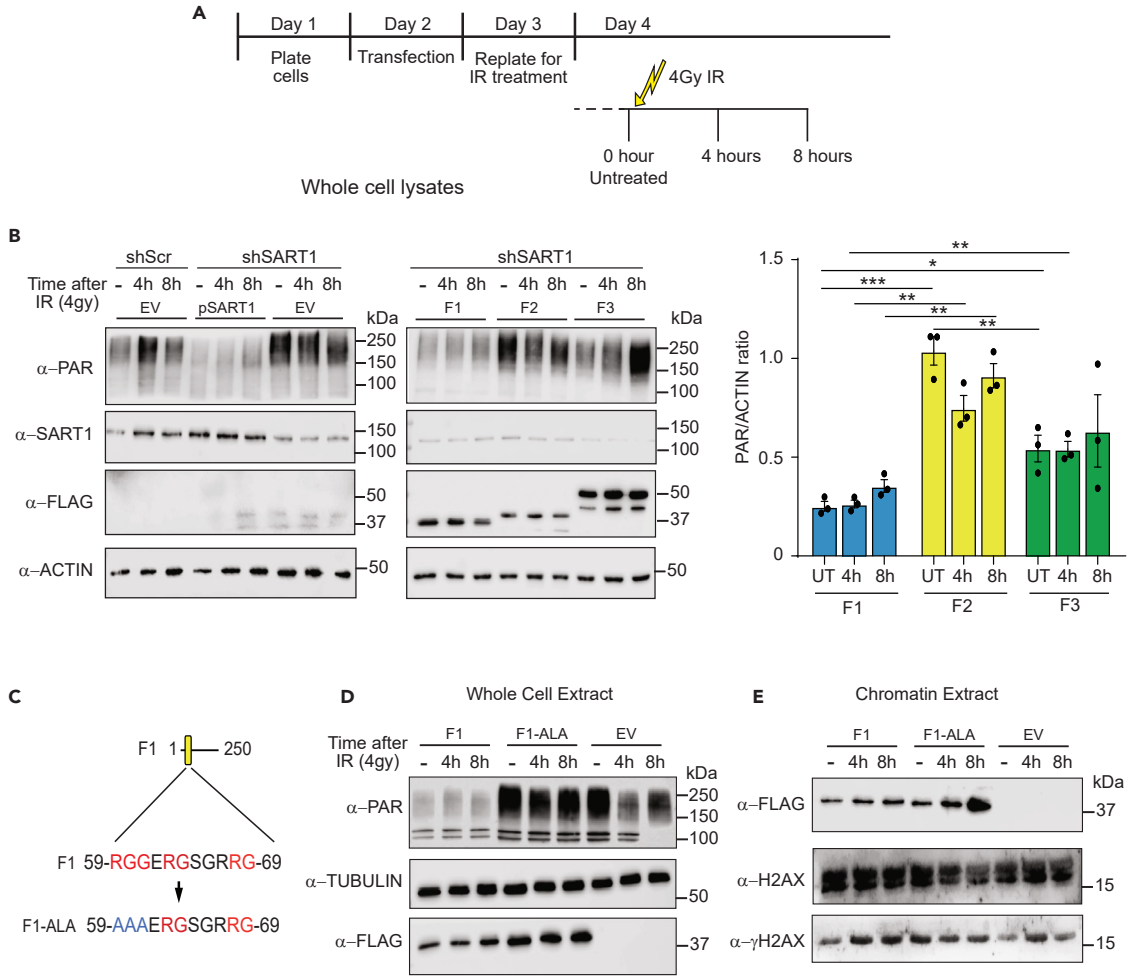

Figure 5. SART1 fragments effect on chromatin localization and PARylation activity

(A) Experimental design to analyze SART1 fragments effect on PARylation. UWB cells silenced for SART1 with a shRNA targeting the 3'UTR of the sequence were seeded on day 1. The next day cells were transfected with a plasmid expressing either a SART1 fragment, a silencing-resistant full-length protein, or with an empty plasmid. On day 3, cells were reseeded. On day 4, they were mock-treated or irradiated with 4 Gy IR and collected at 4 h and 8 h after IR.

(B) PAR chains in samples transfected with empty plasmid, full-length SART1, or SART1 fragment in presence or absence of DNA damage. PAR levels were evaluated using an anti-PAR antibody and their intensity was measured using ImageJ software. Data are shown as mean ± SE of three independent experiments and analyzed with Student's t test. *$p < 0.05$, **$p < 0.01$, ***$p < 0.001$. If not noted, the difference was not significant.

(C) Mutagenesis of first RGG sequence in F1.

(D and E) PAR chains in samples transfected with SART1 F1, mutated F1 (F1-ALA) and empty plasmid in presence or absence of DNA damage. UWB cells silenced for SART1 and transfected with SART1 F1, mutated F1 (F1-ALA) and empty plasmid were irradiated with 4 Gy of IR and collected at 4 h and 8 h after IR. PAR levels were evaluated using an anti-PAR antibody. Fragment expression has been evaluated with anti-FLAG antibody and anti-tubulin as loading control. An anti-γH2AX antibody has been used to visualize DNA damage and an anti-H2AX antibody has been used as loading control. Whole cell (D) and chromatin (E) extracts.

SART1 depletion decreases PARP1 protein levels while increasing PAR levels in whole cell lysates. This imbalance could be due to downregulation of PARG activity, or to an increase of nucleoplasm and chromatin-bound catalytically active PARP1, compensating for the observed reduction of PARP1 levels in the context of SART1 downregulation. Further experiments will be necessary to determine the mechanism for this modulation.

SART1 also co-localizes with PARP1 at stressed replication forks.[51] Treatment with IR induces the accumulation of SART1 in the nucleus and promotes interaction with the PARP1 BRCT domain. Our experiments with SART1 fragments suggest that this interaction involves the cooperativity between the DNA damage-dependent (C-terminal) and -independent (N-terminal) interactions. The N-terminal fragment is sufficient to regulate the accumulation of PAR chains and PARP1 on chromatin, an activity dependent on the RG/RGG-rich motif, but largely independent of DNA damage. We hypothesize that SART1 acts to dampen PARP1 basal activity in normal conditions. Upon DNA damage, the increase in PARP1 activity and chromatin association is followed by an accumulation of SART1 on chromatin, presumably mediated by its C-terminal region, accompanied by dissociation of PARP1 from the chromatin and return of PAR accumulation to pre-damage levels.

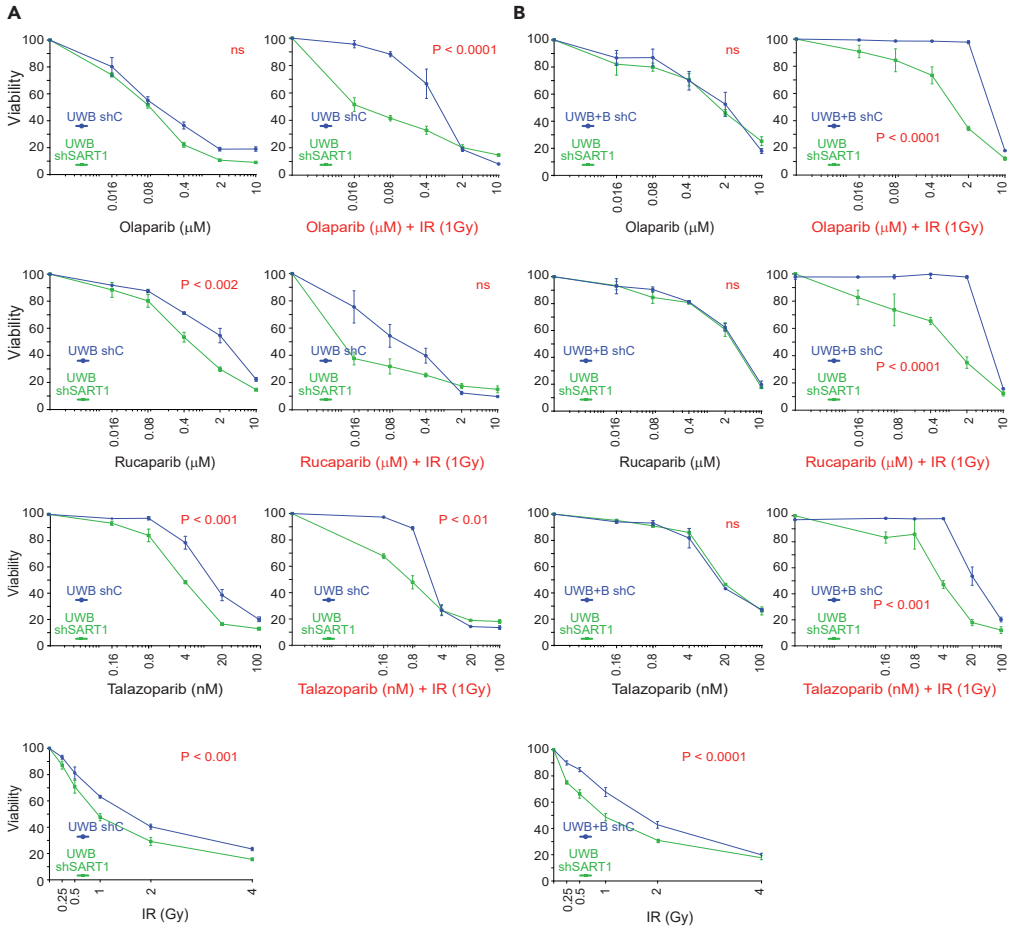

Figure 6. Sensitivity of UWB and UWB+BRCA1 cell lines deficient or proficient for SART1 to different PARP inhibitors and to IR

Clonogenic assays for UWB (A) or UWB+B (B) proficient (control shRNA, shC) or deficient for SART1 (*SART1*-targeting shRNA, shSART1) (blue and green lines, respectively) treated with Olaparib and Rucaparib at concentrations 0 (vehicle), 0.016, 0.08, 0.4, 2, 10 μM, Talazoparib at concentrations 0 (vehicle), 0.16, 0.8, 4, 20, 100 nM for 10 days, in the presence or absence of IR (1 Gy). Viability after IR treatment was measured at doses 0, 0.25, 0.5, 1, 2, 4 Gy. Results from cells treated with PARPi and IR were normalized using the sample treated with IR only. Data are shown as mean ± SD of three independent experiments. Areas under the curve (AUCs) were calculated and compared with a t test (*p* values are indicated; ns, not significant).

SART1 is predicted to contain a disordered region in its N-terminal region and a mechanism for disordered proteins containing RG/RGG-rich motifs to recognize and bind PAR has been suggested[52] and may involve the formation of membrane-less compartments at DNA lesions by liquid demixing,[53] but additional experiments are needed to determine whether SART1 uses a similar mechanism.

The identification of SART1 via tandem affinity purification using only the PARP1 BRCT as bait suggests that this domain is important for the interaction with SART1 although it does not rule out the possibility that other regions of PARP1 contribute to stabilize it. Interestingly, several auto-PARylation sites have been identified in regions flanking or at the BRCT domain,[54] raising the possibility that PAR polymers could modulate the PARP1:SART1 interaction. Further experiments will be necessary to dissect the role of PARP1 domains in SART1 function and whether the interaction is direct or mediated by DNA/RNA or other proteins.

Importantly, silencing of *SART1* led to an increased sensitivity of cells to DNA damage induced by IR irrespective of *BRCA1* status and to PARPis only in absence of *BRCA1*. The effects of short-term *SART1* silencing on cell viability after PARPi treatment is modest and only robustly detected in *BRCA*-deficient cells, which may limit its clinical applicability. However, these experiments were performed on a backdrop of incomplete silencing and relative short PARPi treatment, which may lead to an underestimate of its effects. Furthermore, it is not unusual that even knock-out of genes coding for proteins that modulate the DDR, presumably due to redundancy, causes modest effects with more robust effects only obtained with disruption of additional genes.[55] It is unclear what the mechanism underlying increased sensitivity is. Our results, similar to those obtained by Kim et al.,[50] lead us to hypothesize that a shift from error-free to error-prone in cells silenced for *SART1* repair may contribute to this effect. However, further experiments directly measuring HR and NHEJ are needed to test this hypothesis. PARP1 has been implicated in R-loop resolution[56] and RNA can be used as template for DSB repair.[16] Therefore, SART1 could be involved in these PARP1-related mechanisms and influence DNA repair efficiency. Recently, several positive and negative regulators of

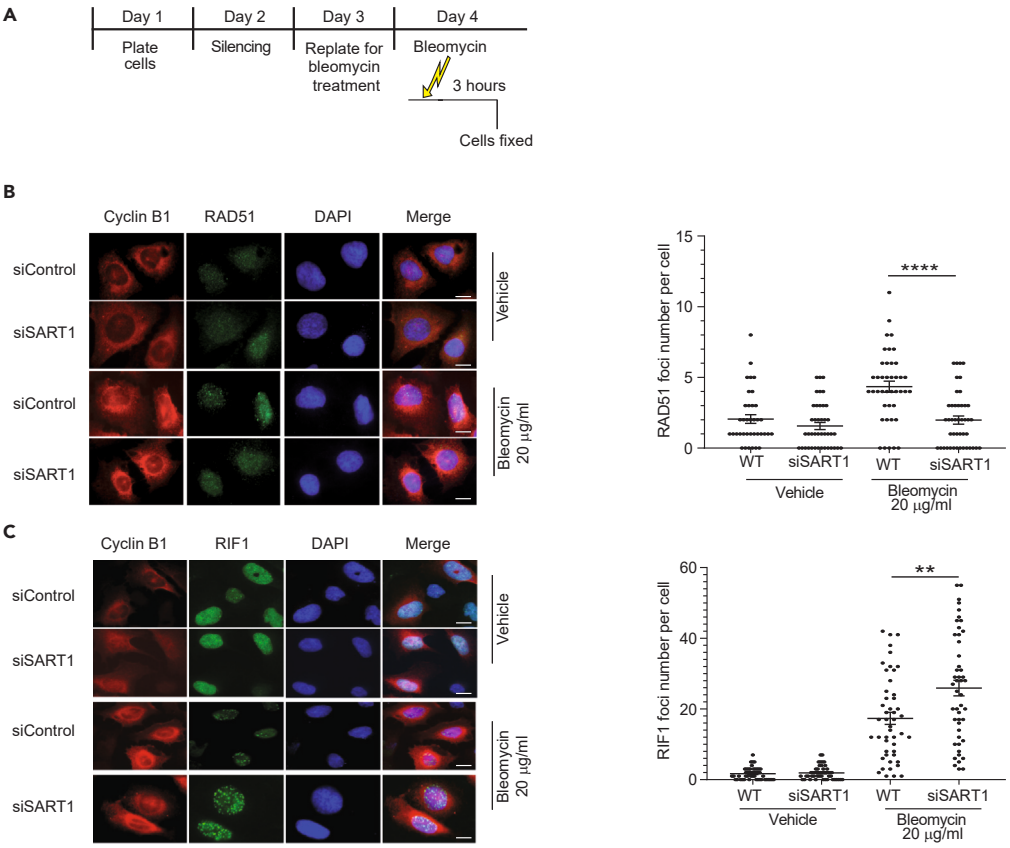

Figure 7. Assessment of DNA repair efficiency

(A) Experimental design to assess choice of DNA repair pathway (homologous recombination or non-homologous end-joining) in *SART1*-deficient and -proficient cells. HeLa cells were seeded and transfected with a siRNA targeting *SART1* or with a non-targeting siRNA on Day 1. On Day 3, cells were reseeded and on Day 4 cells were mock-treated or treated with bleomycin.

(B and C) After fixation, cells were stained for cyclin B1, DAPI, and RAD51 or RIF1 using immunofluorescence and the number of bleomycin-induced RAD51 (B) or RIF1 (C) nuclear foci was quantified. Scale bar, 1 μm. Data are shown as mean ± SD of three independent experiments and analyzed with a t test. $^{**}p < 0.01$, $^{****}p < 0.0001$.

PARP1 activity have been identified displaying a variety of different mechanisms.[57] Interestingly, some regulators are, like SART1, involved in RNA metabolism (e.g., SNORA73, SNORA74A) or alternative splicing after DNA damage (e.g., EWS).[57,58] Further studies will be necessary to dissect the mechanism of SART1 regulation of PARP1, PARPi sensitivity, and the clinical applicability of SART1 downregulation.

The role of SART1 in modulation of repair is supported by its identification in transcriptomics analysis of clinical samples, as a determinant of sensitivity to 5FU and SN38.[33] These results, together with the significant fraction of ovarian tumors that overexpress SART1, suggest that its downregulation could be clinically exploited to improve PARPi efficacy in ovarian cancer as an additional mechanism-based biomarker of PARPi response or as a target to further sensitize *BRCA*-deficient tumors to PARPis.

Limitations of the study

Limitations to our study are that experiments were conducted with partial but not complete depletion of SART1 levels and that we focus on ovarian cancer cell lines. Attempts to generate *SART1*-knock out in UWB1.289 cells failed, consistent with findings that SART1 is an essential protein.[59,60] Further studies will be necessary to validate the generalizability of our findings to other cancers and to extend the analysis to earlier events (e.g., before 1 h after DNA damage). Another limitation was the use of relatively high levels of IR in the TAP-MS experiments. Although samples were collected at an early time point (2 h) after IR exposure, it is possible that some interactions identified may have been triggered by activation of cell death pathways.

RESOURCE AVAILABILITY

Lead contact

Further information and request for resources and reagents should be directed and will be fulfilled by the lead contact, Dr. Alvaro N.A. Monteiro (Alvaro.Monteiro@moffitt.org).

Material availability

The unique reagents generated in this study are available from the lead contact upon request.

Data and code availability

- The published article includes all the functional datasets generated or analyzed during this study. The proteomics datasets have been deposited to the ProteomeXchange Consortium via the PRIDE[61] partner repository with the project accession number PXD047970 (Project DOI: 10.6019/PXD047970). All data reported in this paper will be shared by the lead contact upon request.
- This paper does not report original code.
- Any additional information required to reanalyze the data reported in this paper is available from the lead contact upon request.

ACKNOWLEDGMENTS

This project was supported by the European Union's Horizon 2020 research and innovation programme under the Marie Sklodowska-Curie grant agreement no 842979 (to S.L.), NIH/NCI R21 CA252373 (to A.N.A.M. and U.R.), Associazione Italiana Ricerca sul Cancro (AIRC_IG19917 to A.P.), and the Sarasota Innovation Fund/Moffitt Foundation (to A.N.A.M. and U.R.). A.N.A.M. is a Breast Cancer Research Foundation (BCRF) investigator. The Analytical Microscopy, Proteomics and Metabolomics, and Molecular Genomics cores are supported in part by an NCI Cancer Center Support Grant (P30-CA076292). Immunofluorescence analysis was performed in part at the Unitech NOLIMITS microscopy platform of the Dipartimento di Bioscienze, Università degli Studi di Milano.

AUTHOR CONTRIBUTIONS

Conceptualization: S.L. and A.N.A.M. data curation: S.L., N.T.W., and J.M.K. resources: S.L., N.T.W., and J.M.K. formal analysis: S.L., T.C.N., N.T.W., J.M.K., and A.N.A.M. funding acquisition: S.L., U.R., A.P., and A.N.A.M. investigation: S.L., T.C.N., N.T.W., J.M.K., U.R., and A.N.A.M. visualization: S.L., N.T.W., and A.N.A.M. supervision: A.P. and A.N.A.M. writing original draft: S.L. and A.N.A.M. writing review and editing: all authors.

DECLARATION OF INTERESTS

The authors state that they have no conflict of interest to disclose.

STAR★METHODS

Detailed methods are provided in the online version of this paper and include the following:

SUPPLEMENTAL INFORMATION

Supplemental information can be found online at https://doi.org/10.1016/j.isci.2024.111252.

Received: March 15, 2023
Revised: February 23, 2024
Accepted: October 22, 2024
Published: October 24, 2024

REFERENCES

1. Ray Chaudhuri, A., and Nussenzweig, A. (2017). The multifaceted roles of PARP1 in DNA repair and chromatin remodelling. Nat. Rev. Mol. Cell Biol. *18*, 610–621. https://doi.org/10.1038/nrm.2017.53.
2. Perina, D., Mikoč, A., Ahel, J., Ćetković, H., Žaja, R., and Ahel, I. (2014). Distribution of protein poly(ADP-ribosyl)ation systems across all domains of life. DNA Repair *23*, 4–16. https://doi.org/10.1016/j.dnarep.2014.05.003.
3. Jelinic, P., and Levine, D.A. (2014). New insights into PARP inhibitors' effect on cell cycle and homology-directed DNA damage repair. Mol. Cancer Ther. *13*, 1645–1654. https://doi.org/10.1158/1535-7163.MCT-13-0906-T.
4. Kim, D.S., Challa, S., Jones, A., and Kraus, W.L. (2020). PARPs and ADP-ribosylation in RNA biology: from RNA expression and processing to protein translation and proteostasis. Genes Dev. *34*, 302–320. https://doi.org/10.1101/gad.334433.119.
5. Huang, D., and Kraus, W.L. (2022). The expanding universe of PARP1-mediated molecular and therapeutic mechanisms. Mol. Cell *82*, 2315–2334. https://doi.org/10.1016/j.molcel.2022.02.021.
6. Bonfiglio, J.J., Fontana, P., Zhang, Q., Colby, T., Gibbs-Seymour, I., Atanassov, I., Bartlett, E., Zaja, R., Ahel, I., and Matic, I. (2017). Serine ADP-Ribosylation Depends on HPF1. Mol.

Cell *65*, 932–940.e6. https://doi.org/10.1016/j.molcel.2017.01.003.
7. Hendriks, I.A., Larsen, S.C., and Nielsen, M.L. (2019). An Advanced Strategy for Comprehensive Profiling of ADP-ribosylation Sites Using Mass Spectrometry-based Proteomics. Mol. Cell. Proteomics *18*, 1010–1026. https://doi.org/10.1074/mcp.TIR119.001315.
8. Buch-Larsen, S.C., Hendriks, I.A., Lodge, J.M., Rykær, M., Furtwängler, B., Shishkova, E., Westphall, M.S., Coon, J.J., and Nielsen, M.L. (2020). Mapping Physiological ADP-Ribosylation Using Activated Ion Electron Transfer Dissociation. Cell Rep. *32*, 108176. https://doi.org/10.1016/j.celrep.2020.108176.
9. Wei, H., and Yu, X. (2016). Functions of PARylation in DNA Damage Repair Pathways. Dev. Reprod. Biol. *14*, 131–139. https://doi.org/10.1016/j.gpb.2016.05.001.
10. Dawicki-McKenna, J.M., Langelier, M.F., DeNizio, J.E., Riccio, A.A., Cao, C.D., Karch, K.R., McCauley, M., Steffen, J.D., Black, B.E., and Pascal, J.M. (2015). PARP-1 Activation Requires Local Unfolding of an Autoinhibitory Domain. Mol. Cell *60*, 755–768. https://doi.org/10.1016/j.molcel.2015.10.013.
11. Zhang, Y., Wang, J., Ding, M., and Yu, Y. (2013). Site-specific characterization of the Asp- and Glu-ADP-ribosylated proteome. Nat. Methods *10*, 981–984. https://doi.org/10.1038/nmeth.2603.
12. Larsen, S.C., Hendriks, I.A., Lyon, D., Jensen, L.J., and Nielsen, M.L. (2018). Systems-wide Analysis of Serine ADP-Ribosylation Reveals Widespread Occurrence and Site-Specific Overlap with Phosphorylation. Cell Rep. *24*, 2493–2505.e4. https://doi.org/10.1016/j.celrep.2018.07.083.
13. Leslie Pedrioli, D.M., Leutert, M., Bilan, V., Nowak, K., Gunasekera, K., Ferrari, E., Imhof, R., Malmström, L., and Hottiger, M.O. (2018). Comprehensive ADP-ribosylome analysis identifies tyrosine as an ADP-ribose acceptor site. EMBO Rep. *19*, e45310. https://doi.org/10.15252/embr.201745310.
14. Suskiewicz, M.J., Zobel, F., Ogden, T.E.H., Fontana, P., Ariza, A., Yang, J.C., Zhu, K., Bracken, L., Hawthorne, W.J., Ahel, D., et al. (2020). HPF1 completes the PARP active site for DNA damage-induced ADP-ribosylation. Nature *579*, 598–602. https://doi.org/10.1038/s41586-020-2013-6.
15. Teloni, F., and Altmeyer, M. (2016). Readers of poly(ADP-ribose): designed to be fit for purpose. Nucleic Acids Res. *44*, 993–1006. https://doi.org/10.1093/nar/gkv1383.
16. Bader, A.S., Hawley, B.R., Wilczynska, A., and Bushell, M. (2020). The roles of RNA in DNA double-strand break repair. Br. J. Cancer *122*, 613–623. https://doi.org/10.1038/s41416-019-0624-1.
17. Dziadkowiec, K.N., Gąsiorowska, E., Nowak-Markwitz, E., and Jankowska, A. (2016). PARP inhibitors: review of mechanisms of action and BRCA1/2 mutation targeting. Prz Menopauzalny *15*, 215–219. https://doi.org/10.5114/pm.2016.65667.
18. Ohmoto, A., and Yachida, S. (2017). Current status of poly(ADP-ribose) polymerase inhibitors and future directions. OncoTargets Ther. *10*, 5195–5208. https://doi.org/10.2147/OTT.S139336.
19. Lodovichi, S., Quadri, R., Sertic, S., and Pellicioli, A. (2023). PARylation of BRCA1 limits DNA break resection through BRCA2 and EXO1. Cell Rep. *42*, 112060. https://doi.org/10.1016/j.celrep.2023.112060.
20. Dias, M.P., Moser, S.C., Ganesan, S., and Jonkers, J. (2021). Understanding and overcoming resistance to PARP inhibitors in cancer therapy. Nat. Rev. Clin. Oncol. *18*, 773–791. https://doi.org/10.1038/s41571-021-00532-x.
21. Zheng, F., Zhang, Y., Chen, S., Weng, X., Rao, Y., and Fang, H. (2020). Mechanism and current progress of Poly ADP-ribose polymerase (PARP) inhibitors in the treatment of ovarian cancer. Biomed. Pharmacother. *123*, 109661. https://doi.org/10.1016/j.biopha.2019.109661.
22. Rose, M., Burgess, J.T., O'Byrne, K., Richard, D.J., and Bolderson, E. (2020). PARP Inhibitors: Clinical Relevance, Mechanisms of Action and Tumor Resistance. Front. Cell Dev. Biol. *8*, 564601. https://doi.org/10.3389/fcell.2020.564601.
23. Sandhu, S.K., Schelman, W.R., Wilding, G., Moreno, V., Baird, R.D., Miranda, S., Hylands, L., Riisnaes, R., Forster, M., Omlin, A., et al. (2013). The poly(ADP-ribose) polymerase inhibitor niraparib (MK4827) in BRCA mutation carriers and patients with sporadic cancer: a phase 1 dose-escalation trial. Lancet Oncol. *14*, 882–892. https://doi.org/10.1016/S1470-2045(13)70240-7.
24. Audeh, M.W., Carmichael, J., Penson, R.T., Friedlander, M., Powell, B., Bell-McGuinn, K.M., Scott, C., Weitzel, J.N., Oaknin, A., Loman, N., et al. (2010). Oral poly(ADP-ribose) polymerase inhibitor olaparib in patients with BRCA1 or BRCA2 mutations and recurrent ovarian cancer: a proof-of-concept trial. Lancet *376*, 245–251. https://doi.org/10.1016/S0140-6736(10)60893-8.
25. Mohyuddin, G.R., Aziz, M., Britt, A., Wade, L., Sun, W., Baranda, J., Al-Rajabi, R., Saeed, A., and Kasi, A. (2020). Similar response rates and survival with PARP inhibitors for patients with solid tumors harboring somatic versus Germline BRCA mutations: a Meta-analysis and systematic review. BMC Cancer *20*, 507. https://doi.org/10.1186/s12885-020-06948-5.
26. Oza, A.M., Tinker, A.V., Oaknin, A., Shapira-Frommer, R., McNeish, I.A., Swisher, E.M., Ray-Coquard, I., Bell-McGuinn, K., Coleman, R.L., O'Malley, D.M., et al. (2017). Antitumor activity and safety of the PARP inhibitor rucaparib in patients with high-grade ovarian carcinoma and a germline or somatic BRCA1 or BRCA2 mutation: Integrated analysis of data from Study 10 and ARIEL2. Gynecol. Oncol. *147*, 267–275. https://doi.org/10.1016/j.ygyno.2017.08.022.
27. D'Andrea, A.D. (2018). Mechanisms of PARP inhibitor sensitivity and resistance. DNA Repair *71*, 172–176. https://doi.org/10.1016/j.dnarep.2018.08.021.
28. Miller, R.E., Leary, A., Scott, C.L., Serra, V., Lord, C.J., Bowtell, D., Chang, D.K., Garsed, D.W., Jonkers, J., Ledermann, J.A., et al. (2020). ESMO recommendations on predictive biomarker testing for homologous recombination deficiency and PARP inhibitor benefit in ovarian cancer. Ann. Oncol. *31*, 1606–1622. https://doi.org/10.1016/j.annonc.2020.08.2102.
29. La Ferla, M., Mercatanti, A., Rocchi, G., Lodovichi, S., Cervelli, T., Pignata, L., Caligo, M.A., and Galli, A. (2015). Expression of human poly (ADP-ribose) polymerase 1 in Saccharomyces cerevisiae: Effect on survival, homologous recombination and identification of genes involved in intracellular localization. Mutat. Res. *774*, 14–24. https://doi.org/10.1016/j.mrfmmm.2015.02.006.
30. Palve, V., Knezevic, C.E., Bejan, D.S., Luo, Y., Li, X., Novakova, S., Welsh, E.A., Fang, B., Kinose, F., Haura, E.B., et al. (2022). The non-canonical target PARP16 contributes to polypharmacology of the PARP inhibitor talazoparib and its synergy with WEE1 inhibitors. Cell Chem. Biol. *29*, 202–214.e7. https://doi.org/10.1016/j.chembiol.2021.07.008.
31. Shichijo, S., Nakao, M., Imai, Y., Takasu, H., Kawamoto, M., Niiya, F., Yang, D., Toh, Y., Yamana, H., and Itoh, K. (1998). A gene encoding antigenic peptides of human squamous cell carcinoma recognized by cytotoxic T lymphocytes. J. Exp. Med. *187*, 277–288. https://doi.org/10.1084/jem.187.3.277.
32. Makarova, O.V., Makarov, E.M., and Lührmann, R. (2001). The 65 and 110 kDa SR-related proteins of the U4/U6.U5 tri-snRNP are essential for the assembly of mature spliceosomes. EMBO J. *20*, 2553–2563. https://doi.org/10.1093/emboj/20.10.2553.
33. Allen, W.L., Stevenson, L., Coyle, V.M., Jithesh, P.V., Proutski, I., Carson, G., Gordon, M.A., Lenz, H.J.D., Van Schaeybroeck, S., Longley, D.B., and Johnston, P.G. (2012). A systems biology approach identifies SART1 as a novel determinant of both 5-fluorouracil and SN38 drug resistance in colorectal cancer. Mol. Cancer Ther. *11*, 119–131. https://doi.org/10.1158/1535-7163.MCT-11-0510.
34. Woods, N.T., Mesquita, R.D., Sweet, M., Carvalho, M.A., Li, X., Liu, Y., Nguyen, H., Thomas, C.E., Iversen, E.S., Jr., Marsillac, S., et al. (2012). Charting the landscape of tandem BRCT domain-mediated protein interactions. Sci. Signal. *5*, rs6. https://doi.org/10.1126/scisignal.2002255.
35. Mohammad, D.H., and Yaffe, M.B. (2009). 14-3-3 proteins, FHA domains and BRCT domains in the DNA damage response. DNA Repair *8*, 1009–1017.
36. Tao, Z., Gao, P., and Liu, H.W. (2009). Studies of the expression of human poly(ADP-ribose) polymerase-1 in Saccharomyces cerevisiae and identification of PARP-1 substrates by yeast proteome microarray screening. Biochemistry *48*, 11745–11754. https://doi.org/10.1021/bi901387k.
37. Kliza, K.W., Liu, Q., Roosenboom, L.W.M., Jansen, P.W.T.C., Filippov, D.V., and Vermeulen, M. (2021). Reading ADP-ribosylation signaling using chemical biology and interaction proteomics. Mol. Cell *81*, 4552–4567.e8. https://doi.org/10.1016/j.molcel.2021.08.037.
38. Hendriks, I.A., Buch-Larsen, S.C., Prokhorova, E., Elsborg, J.D., Rebak, A.K.L.F.S., Zhu, K., Ahel, D., Lukas, C., Ahel, I., and Nielsen, M.L. (2021). The regulatory landscape of the human HPF1- and ARH3-dependent ADP-ribosylome. Nat. Commun. *12*, 5893. https://doi.org/10.1038/s41467-021-26172-4.
39. Behan, F.M., Iorio, F., Picco, G., Gonçalves, E., Beaver, C.M., Migliardi, G., Santos, R., Rao, Y., Sassi, F., Pinnelli, M., et al. (2019). Prioritization of cancer therapeutic targets using CRISPR-Cas9 screens. Nature *568*, 511–516. https://doi.org/10.1038/s41586-019-1103-9.
40. Hart, T., Chandrashekhar, M., Aregger, M., Steinhart, Z., Brown, K.R., MacLeod, G., Mis, M., Zimmermann, M., Fradet-Turcotte, A., Sun, S., et al. (2015). High-Resolution CRISPR Screens Reveal Fitness Genes and Genotype-Specific Cancer Liabilities. Cell *163*, 1515–

1526. https://doi.org/10.1016/j.cell.2015.11.015.

41. Huang, A., Garraway, L.A., Ashworth, A., and Weber, B. (2020). Synthetic lethality as an engine for cancer drug target discovery. Nat. Rev. Drug Discov. *19*, 23–38. https://doi.org/10.1038/s41573-019-0046-z.
42. Deng, O., Dash, S., Nepomuceno, T.C., Fang, B., Yun, S.Y., Welsh, E.A., Lawrence, H.R., Marchion, D., Koomen, J.M., Monteiro, A.N., and Rix, U. (2022). Integrated proteomics identifies PARP inhibitor-induced prosurvival signaling changes as potential vulnerabilities in ovarian cancer. J. Biol. Chem. *298*, 102550. https://doi.org/10.1016/j.jbc.2022.102550.
43. Murai, J., Huang, S.Y., Das, B.B., Renaud, A., Zhang, Y., Doroshow, J.H., Ji, J., Takeda, S., and Pommier, Y. (2012). Trapping of PARP1 and PARP2 by Clinical PARP Inhibitors. Cancer Res. *72*, 5588–5599. https://doi.org/10.1158/0008-5472.CAN-12-2753.
44. Coelho, R., Tozzi, A., Disler, M., Lombardo, F., Fedier, A., López, M.N., Freuler, F., Jacob, F., and Heinzelmann-Schwarz, V. (2022). Overlapping gene dependencies for PARP inhibitors and carboplatin response identified by functional CRISPR-Cas9 screening in ovarian cancer. Cell Death Dis. *13*, 909. https://doi.org/10.1038/s41419-022-05347-x.
45. Lodovichi, S., Cervelli, T., Pellicioli, A., and Galli, A. (2020). Inhibition of DNA Repair in Cancer Therapy: Toward a Multi-Target Approach. Int. J. Mol. Sci. *21*, 6684. https://doi.org/10.3390/ijms21186684.
46. Ngoi, N.Y.L., Westin, S.N., and Yap, T.A. (2022). Targeting the DNA damage response beyond poly(ADP-ribose) polymerase inhibitors: novel agents and rational combinations. Curr. Opin. Oncol. *34*, 559–569. https://doi.org/10.1097/CCO.0000000000000867.
47. Polo, S.E., Blackford, A.N., Chapman, J.R., Baskcomb, L., Gravel, S., Rusch, A., Thomas, A., Blundred, R., Smith, P., Kzhyshkowska, J., et al. (2012). Regulation of DNA-end resection by hnRNPU-like proteins promotes DNA double-strand break signaling and repair. Mol. Cell *45*, 505–516. https://doi.org/10.1016/j.molcel.2011.12.035.
48. Mastrocola, A.S., Kim, S.H., Trinh, A.T., Rodenkirch, L.A., and Tibbetts, R.S. (2013). The RNA-binding protein fused in sarcoma (FUS) functions downstream of poly(ADP-ribose) polymerase (PARP) in response to DNA damage. J. Biol. Chem. *288*, 24731–24741. https://doi.org/10.1074/jbc.M113.497974.
49. Hong, Z., Jiang, J., Ma, J., Dai, S., Xu, T., Li, H., and Yasui, A. (2013). The role of hnRPUL1 involved in DNA damage response is related to PARP1. PLoS One *8*, e60208. https://doi.org/10.1371/journal.pone.0060208.
50. Kim, J.J., Lee, S.Y., Hwang, Y., Kim, S., Chung, J.M., Park, S., Yoon, J., Yun, H., Ji, J.H., Chae, S., et al. (2021). USP39 promotes non-homologous end-joining repair by poly(ADP-ribose)-induced liquid demixing. Nucleic Acids Res. *49*, 11083–11102. https://doi.org/10.1093/nar/gkab892.
51. Mosler, T., Baymaz, H.I., Gräf, J.F., Mikicic, I., Blattner, G., Bartlett, E., Ostermaier, M., Piccinno, R., Yang, J., Voigt, A., et al. (2022). PARP1 proximity proteomics reveals interaction partners at stressed replication forks. Nucleic Acids Res. *50*, 11600–11618. https://doi.org/10.1093/nar/gkac948.
52. Fischbach, A., Krüger, A., Hampp, S., Assmann, G., Rank, L., Hufnagel, M., Stöckl, M.T., Fischer, J.M.F., Veith, S., Rossatti, P., et al. (2018). The C-terminal domain of p53 orchestrates the interplay between non-covalent and covalent poly(ADP-ribosyl)ation of p53 by PARP1. Nucleic Acids Res. *46*, 804–822. https://doi.org/10.1093/nar/gkx1205.
53. Altmeyer, M., Neelsen, K.J., Teloni, F., Pozdnyakova, I., Pellegrino, S., Grøfte, M., Rask, M.B.D., Streicher, W., Jungmichel, S., Nielsen, M.L., and Lukas, J. (2015). Liquid demixing of intrinsically disordered proteins is seeded by poly(ADP-ribose). Nat. Commun. *6*, 8088. https://doi.org/10.1038/ncomms9088.
54. Ayyappan, V., Wat, R., Barber, C., Vivelo, C.A., Gauch, K., Visanpattanasin, P., Cook, G., Sazeides, C., and Leung, A.K.L. (2021). ADPriboDB 2.0: an updated database of ADP-ribosylated proteins. Nucleic Acids Res. *49*, D261–D265. https://doi.org/10.1093/nar/gkaa941.
55. Fugger, K., Bajrami, I., Silva Dos Santos, M., Young, S.J., Kunzelmann, S., Kelly, G., Hewitt, G., Patel, H., Goldstone, R., Carell, T., et al. (2021). Targeting the nucleotide salvage factor DNPH1 sensitizes BRCA-deficient cells to PARP inhibitors. Science *372*, 156–165. https://doi.org/10.1126/science.abb4542.
56. Laspata, N., Kaur, P., Mersaoui, S.Y., Muoio, D., Liu, Z.S., Bannister, M.H., Nguyen, H.D., Curry, C., Pascal, J.M., Poirier, G.G., et al. (2023). PARP1 associates with R-loops to promote their resolution and genome stability. Nucleic Acids Res. *51*, 2215–2237. https://doi.org/10.1093/nar/gkad066.
57. Zhu, T., Zheng, J.Y., Huang, L.L., Wang, Y.H., Yao, D.F., and Dai, H.B. (2023). Human PARP1 substrates and regulators of its catalytic activity: An updated overview. Front. Pharmacol. *14*, 1137151. https://doi.org/10.3389/fphar.2023.1137151.
58. Paronetto, M.P., Miñana, B., and Valcárcel, J. (2011). The Ewing sarcoma protein regulates DNA damage-induced alternative splicing. Mol. Cell *43*, 353–368. https://doi.org/10.1016/j.molcel.2011.05.035.
59. Wang, T., Birsoy, K., Hughes, N.W., Krupczak, K.M., Post, Y., Wei, J.J., Lander, E.S., and Sabatini, D.M. (2015). Identification and characterization of essential genes in the human genome. Science *350*, 1096–1101. https://doi.org/10.1126/science.aac7041.
60. Koh, M.Y., Gagea, M., Sargis, T., Lemos, R., Jr., Grandjean, G., Charbono, A., Bekiaris, V., Sedy, J., Kiriakova, G., Liu, X., et al. (2016). A new HIF-1alpha/RANTES-driven pathway to hepatocellular carcinoma mediated by germline haploinsufficiency of SART1/HAF in mice. Hepatology *63*, 1576–1591. https://doi.org/10.1002/hep.28468.
61. Vizcaíno, J.A., Csordas, A., Del-Toro, N., Dianes, J.A., Griss, J., Lavidas, I., Mayer, G., Perez-Riverol, Y., Reisinger, F., Ternent, T., et al. (2016). 2016 update of the PRIDE database and its related tools. Nucleic Acids Res. *44*, 11033. https://doi.org/10.1093/nar/gkw880.
62. Swift, S., Lorens, J., Achacoso, P., and Nolan, G.P. (2001). Rapid production of retroviruses for efficient gene delivery to mammalian cells using 293T cell-based systems. Curr. Protoc. Immunol. *31*, 10–17. https://doi.org/10.1002/0471142735.im1017cs31.
63. Keller, A., Nesvizhskii, A.I., Kolker, E., and Aebersold, R. (2002). Empirical statistical model to estimate the accuracy of peptide identifications made by MS/MS and database search. Anal. Chem. *74*, 5383–5392.
64. Nesvizhskii, A.I., Keller, A., Kolker, E., and Aebersold, R. (2003). A statistical model for identifying proteins by tandem mass spectrometry. Anal. Chem. *75*, 4646–4658.
65. Choi, H., Larsen, B., Lin, Z.Y., Breitkreutz, A., Mellacheruvu, D., Fermin, D., Qin, Z.S., Tyers, M., Gingras, A.C., and Nesvizhskii, A.I. (2011). SAINT: probabilistic scoring of affinity purification-mass spectrometry data. Nat. Methods *8*, 70–73. https://doi.org/10.1038/nmeth.1541.
66. Teo, G., Liu, G., Zhang, J., Nesvizhskii, A.I., Gingras, A.C., and Choi, H. (2014). SAINTexpress: improvements and additional features in Significance Analysis of INTeractome software. J. Proteomics *100*, 37–43. https://doi.org/10.1016/j.jprot.2013.10.023.
67. Mellacheruvu, D., Wright, Z., Couzens, A.L., Lambert, J.P., St-Denis, N.A., Li, T., Miteva, Y.V., Hauri, S., Sardiu, M.E., Low, T.Y., et al. (2013). The CRAPome: a contaminant repository for affinity purification-mass spectrometry data. Nat. Methods *10*, 730–736. https://doi.org/10.1038/nmeth.2557.
68. Bonfiglio, J.J., Leidecker, O., Dauben, H., Longarini, E.J., Colby, T., San Segundo-Acosta, P., Perez, K.A., and Matic, I. (2020). An HPF1/PARP1-Based Chemical Biology Strategy for Exploring ADP-Ribosylation. Cell *183*, 1086–1102.e23. https://doi.org/10.1016/j.cell.2020.09.055.
69. Lex, A., Gehlenborg, N., Strobelt, H., Vuillemot, R., and Pfister, H. (2014). UpSet: Visualization of Intersecting Sets. IEEE Trans. Vis. Comput. Graph. *20*, 1983–1992. https://doi.org/10.1109/TVCG.2014.2346248.

STAR★METHODS

KEY RESOURCES TABLE

REAGENT or RESOURCE	SOURCE	IDENTIFIER
Antibodies		
Rabbit anti-SART1 antibody	Novus Biological	NBP1-89024
Rabbit anti-PARP1 antibody	Cell Signaling	9542
Mouse anti-TUBULIN antibody	Sigma-Aldrich	T5168
Mouse anti-ACTIN antibody	Sigma-Aldrich	A5316
Mouse anti-FLAG antibody	Sigma-Aldrich	F4049
Mouse anti-PAR antibody	RD-Systems	4335-MC-100
Rabbit anti-H2AX antibody	Millipore-Sigma	07–627
Rabbit anti-γH2AX antibody	Millipore-Sigma	07–164
Rabbit anti-LaminB1 antibody	Sigma-Aldrich	SAB1410759
Rabbit anti-RIF1 antibody	Thermo Fischer Scientific	PA5-57857
Rabbit anti-RAD51 antibody	Calbiochem	PC-130
Mouse anti-CYCLIN-B1 antibody	BD pharmingen	554176
Bacterial and Virus Strains		
DH5alpha competent cells	Thermo Fisher Scientific	18265017
Takara Stable Competent Cells	Takara	9132
HIV-1-based lentivirus	Thermo Fischer Scientific	N/A
Chemicals, Peptides, and Recombinant Proteins		
Bleomycin	Merck	B7216
Penicillin-Streptomycin	Euroclone	ECB3001
Puromycin	Thermo Fischer Scientific	A1113802
Formaldehyde	Sigma-Aldrich	P6148
Olaparib	TargetMOL	TMO-T3015
Rucaparib	TargetMOL	TMO-T4463
Talazoparib	TargetMOL	TMO-T6253
HindIII restriction enzyme	NEB	R0104S
XhoI restriction enzyme	NEB	R0146S
RIPA Lysis and Extraction Buffer	Thermo Fischer Scientific	89900
A/G PLUS–agarose beads	Santa-Cruz Biotechnology	sc-2003
ANTI-FLAG ® M2 Affinity Gel	Sigma-Aldrich	A2220
cOmplete™ ULTRA Tablets, Mini, Protease Inhibitor Cocktail	Roche	5892970001
Proteinase K	Amsbio	120493–1
RNase A	Sigma-Aldrich	R6513
ProlongGold with DAPI	Thermo Fischer Scientific	P36931
Trypsin	Promega	V5111
Critical Commercial Assays		
Qiagen Spin Miniprep Kit	Qiagen	27106
FuGENE® HD Transfection Reagent	Promega	E2311
Lipofectamine RNAiMAX Transfection Reagent	Thermo Fischer Scientific	13778150
Lipofectamine 3000 Transfection Reagent	Thermo Fischer Scientific	L3000001
ViraPower™ Lentiviral Packaging Mix	Thermo Fischer Scientific	K4975-00

(*Continued on next page*)

Continued

REAGENT or RESOURCE	SOURCE	IDENTIFIER
NucleoSpin Tissue, Mini kit for DNA from cells and tissue	Macherey-Nagel	740952.250
QuikChange II Site-Directed Mutagenesis Kit	Agilent	200523
Clarity Western ECL Substrate	Biorad	1705061
InterPlay Mammalian TAP Purification Kit	Agilent	240107
Deposited Data		
MS proteomics data	ProteomeXchange Consortium	PXD047970
Experimental Model: *cell lines*		
Human: HEK293T	ATCC	CRL-1573
Human: HEK293FT	ATCC	N/A
Human: HEY A8	ATCC	N/A
Human: UWB1.289	ATCC	CRL-2945
Human: UWB1.289+BRCA1	ATCC	CRL-2946
Human: HeLa	ATCC	CCL-2
Oligonucleotides		
List of oligonucleotides used in the study:	Table S1	N/A
Recombinant DNA		
pCMV6-Entry Expression Vector	Origene	PS100001
pFRT/TO/HIS/FLAG/HA-SART1	Addgene	38087
pLKO-puro-SART1shrnaCDS	Sigma-Aldrich	TRCN0000001088
pLKO-puro-SART1shrnaUTR	Sigma-Aldrich	TRCN0000320692
pLP1	Thermo Fischer Scientific	K4975-00
pLP2	Thermo Fischer Scientific	K4975-00
pLP/VSVG	Thermo Fischer Scientific	K4975-00
pNTAP	Agilent	240101
Software and Algorithms		
ImageJ	https://imagej.nih.gov/ij	N/A
Graph-pad Prism 8	https://www.graphpad.com	N/A
ClustalW	https://www.genome.jp/tools-bin/clustalw	N/A
PrDOS	https://prdos.hgc.jp/	N/A
Other		
Trans-Blot® Turbo™ Transfer System	Bio-Rad	1704150
SP8 Laser Scanning Confocal Microscope	Leica	N/A
LTQ Orbitrap	Thermo Fischer Scientific	BRE725536

EXPERIMENTAL MODEL AND STUDY PARTICIPANT DETAILS

We used the human embryonic kidney cell lines HEK293T and HEK293FT, the cervical cancer cell line HeLa, and human ovarian cancer cell lines HEY A8 and the isogenic pair UWB1.289 (BRCA1-null) and UWB1.289+BRCA1 (BRCA1-reconstituted) obtained from ATCC. HEK293T, HEK293FT, and HeLa cells were maintained in Dulbecco's modified Eagle's medium (DMEM, GIBCO), and HEY A8 cells were maintained in RPMI (GIBCO). Media were supplemented with 10% (v/v) fetal bovine serum (FBS, GIBCO). UWB1.289 and UWB1.289+BRCA1 were maintained in 50% Mammary Epithelial Growth Medium (MEGM Bullet Kit, ATCC) and 50% RPMI-1640 Medium (ATCC) supplemented with 3% (v/v) FBS. All cell lines were cultured at 37°C, 5% CO2 in a humidified incubator and penicillin/streptomycin antibiotics added to each culture media to a final concentration of 1% (v/v). Cell lines were authenticated by Short Tandem Repeat (STR) and preriodically tested for mycoplasma.

METHOD DETAILS

Tandem affinity purification

PARP1 BRCT (aa 375–486) and control GFP constructs were subcloned into the pNTAP vector (Agilent) which contains calmodulin binding peptide and streptavidin binding peptide epitope tags. Transfections were performed using a modified calcium phosphate method.[62] Briefly, 293T cells in 150 mm culture dishes were grown to 40% confluency and transfected with 30 μg vector. Ten hours post transfection, culture medium was replaced with fresh DMEM. After 24 h, cells were exposed to 20 Gy IR or mock treated and incubated for 2 h. Cells were harvested in TAP lysis buffer (aqueous 0.5% Nonidet P-40, 20 mM Tris pH 8.0, 50 mM NaCl, 50 mM NaF, 100 μM Na_3VO_4, 1 mM DTT, and 50 μg/mL PMSF). Lysates contained approximately 1 x 10^8 cells. TAP-tagged PARP1 BRCT and associated protein complexes were purified using the InterPlay TAP purification kit (Agilent) with NETN buffer used for lysis.[34] Lysates were then cleared by centrifugation at 13,000 x *g* for 5 min at 4°C and washed three times with 1 mL of NETN. After elution, the supernatant was heated for 5 min at 95°C with XT sample buffer (Bio-Rad) and subjected to XT-MOPS polyacrylamide gel electrophoresis. Correct folding was inferred from protein stability determined by western blot and through the identification of interactors described in the literature through independent experiments.

Mass spectrometry

Protein fractions were excised from the XT-MOPS gel, cut into 3–5 cubes, washed with deionized water, destained with 1 mL aqueous 50 mM ammonium bicarbonate with 50% MeOH, reduced with 2 mM tris-carboxyethylphosphinein aqueous 50 mM ammonium bicarbonate 2 × 15 min at 37°C, alkylated with 20 mM iodoacetamide in aqueous 50 mM ammonium bicarbonate 2 × 20 min at 37°C in the dark, washed three times with aqueous 50 mM ammonium bicarbonate with 50% MeOH and digested overnight with 200 ng sequencing-grade trypsin (Promega) after rehydration with aqueous 30 mM ammonium bicarbonate in volumes sufficient to keep all of the gel submerged. Tryptic peptides were eluted twice from the gel using 100 μL of aqueous 50% acetonitrile containing 0.1% trifluoroacetic acid and concentrated to 20 μL by vacuum centrifugation. A nanoflow ultra-high-performance liquid chromatograph coupled to interfaced with an electrospray ion trap mass spectrometer (Dionex U3000 and LTQ Orbitrap, Thermo) were used for tandem mass spectrometry (MS/MS) peptide sequencing experiments.

In this study, two independent replicates were run for PARP1 BRCT and four independent replicates were run for TAP-tagged GFP which were used to remove non-specific binding protein contaminants in later analysis using SAINTexpress. All MS/MS samples were analyzed using Mascot (Matrix Science, London, UK; version Mascot) set up to search the Sprot_20130501 database (selected for Homo sapiens, 20330 entries) assuming the digestion enzyme trypsin. Fragment ion mass tolerance of 0.80 Da (for ion trap MS/MS data) and a parent ion tolerance of 1.2 Da (to accommodate selection of the incorrect isotope) were used. Oxidation of methionine and carbamidomethylation \of cysteine were specified in Mascot as variable modifications.

Scaffold (version Scaffold_2_04_00, Proteome Software Inc., Portland, OR) was used to validate MS/MS based peptide and protein identifications and peptide identifications, which were accepted if they had >95.0% probability as specified by the Peptide Prophet algorithm.[63] Protein identifications were accepted if they had >95.0% probability and contained at least one identified peptide. Protein probabilities were assigned by the Protein Prophet algorithm[64] and proteins that contained similar peptides and could not be differentiated based on MS/MS analysis alone were grouped to satisfy the principles of parsimony. The MS proteomics data have been deposited to the ProteomeXchange Consortium via the PRIDE[61] partner repository with the project accession number PXD047970 (Project https://doi.org/10.6019/PXD047970).

SAINTexpress processing and filtering of mass spectrometry data

Total spectral counts for each protein identified by the mass spectrometry processing were used as input into the probabilistic scoring algorithm SAINTexpress (version 3.6.1).[65,66] A total of 289 control datasets were used to calculate the probability of true interactions for each identified protein. The 289 control databases include six TAP-GFP purifications (one mock treated and one IR treated from,[34] two IR treated, and two Sodium Butyrate-treated in this study) and 283 control datasets from the CRAPome (crapome.org).[67] Proteins with a Bayesian False Discovery Rate (BFDR) ≤ 0.05 were considered further. Proteins were excluded from further analysis if they contained gene ontology association of calmodulin binding (GO:0005516), which could arise from non-specific associations with calmodulin beads as part of the TAP purification protocol, or if they were tubulin proteins.

Public databases analysis

We focused our analysis on cancers where PARPis are used in therapy. Information on SART1 expression in normal tissue have been obtained querying GTEx portal (https://gtexportal.org/home/), while data regarding genetic alterations and survival in patients with ovarian, breast, pancreatic and prostate cancer with alteration in *SART1* have been obtained using cBioPortal (https://www.cbioportal.org/) and querying for data from the TCGA database on 10/13/2021 for Ovarian Serous Cystadenocarcinoma (TCGA, Firehose Legacy), $n = 600$; Breast Invasive Carcinoma (TCGA, PanCancer Atlas), $n = 994$; Prostate Adenocarcinoma (TCGA, Firehose Legacy), $n = 491$; Pancreatic Adenocarcinoma (TCGA, Firehose Legacy), $n = 149$. Specifically, we queried by *SART1* gene by searching for samples with CNA and mutation data and selecting genomic profiles with mutations, putative copy-number alterations, and mRNA expression.

Lentiviral transduction for stable silencing

pLKO-puro plasmid expressing shRNAs targeting the coding region or the untranslated region (UTR) of *SART1* were obtained from SIGMA-ALDRICH (Figure S7). pLP1, pLP2, and pLP/VSVG ViraPower (Thermo Fisher) viral packaging vectors were used along with pLKO-puro-SART1shrnaCDS and pLKO-puro-SART1shrnaUTR to make virus particles in HEK293FT cells following the manufacturer's instruction. Virus particles were used to transduce HEK293T, HeLa, HEY A8, UWB1.289 and UWB1.289+BRCA1 cells, followed by 1 μg/mL puromycin selection. Cells were expanded maintaining the puromycin selection, and in every experiment SART1 silencing has been verified by Western blot.

Western blot

Whole cell extracts were obtained lysing cells with NETN buffer (0.5% NP-40, 20 mM Tris pH 8.0, 50 mM NaCl, 50 mM NaF, 100 μM Na_3VO_4, 1 mM DTT) supplemented with 1 × cOmplete, Mini Protease Inhibitor Cocktail (Roche) and 1 mM PMSF for 30 min in ice and then centrifuging extract at 4°C, 15,300 x *g* for 15 min. Supernatants were quantified using Bio-Rad Protein Assay Dye Reagent, following the manufacturer's instructions and ~20 μg of proteins were loaded per lane on polyacrylamide gels ranging from 8% to 12% of acrylamide percentage based on the molecular weight of the protein of interest.

Proteins were transferred to methanol-activated PVDF membrane using the TransBlot Turbo system (Bio-Rad Laboratories, Hercules, California) and membranes were blocked for 1 h at room temperature with 5% skim milk solution prepared in TBS-Tween (0.1%). Membranes were incubated with primary antibodies at 4°C, overnight and with secondary antibodies at room temperature for 1 h. We used the following antibodies: rabbit anti-SART1 (NBP1-89024, Novus Biological), rabbit anti-PARP1 (9542, Cell Signaling), mouse anti-TUBULIN (T5168, Sigma-Aldrich), mouse anti-ACTIN (A5316, Sigma-Aldrich), mouse anti-FLAG (F4049- Sigma-Aldrich), mouse anti-PAR (4335-MC-100, RD-Systems), rabbit anti-H2AX, rabbit anti-γH2AX (07–164, Millipore-Sigma), rabbit anti-LaminB1 (SAB1410759, Sigma-Aldrich), rabbit anti-pAKT (4058, cell signaling), rabbit anti-AKT.

Immunoprecipitation

Immunoprecipitations were performed using 500–1000 μg of whole cell protein extracts. Protein extracts were incubated with 1 μg of primary antibody or anti-IgG antibody, as negative control, together with 30 μL protein A/G PLUS–agarose beads (Santa Cruz Biotechnology) for 2 h at 4°C in a rocking platform. Samples were then centrifuged at 2,000 x *g*, 4°C for 5 min and pellets were washed four times with RIPA buffer (Thermo Fisher Scientific). Finally, proteins were eluted by boiling samples at 100°C for 3 min with 2x Laemmli buffer and 5–10 μL of sample was resolved on poly-acrylamide gel. For pulldown of FLAG-tagged proteins we followed the same protocol using 30 μL of anti-FLAG M2 affinity gel (Sigma-Aldrich, A2220).

For phosphorylation dependency IP experiments, protein extracts were incubated with 1 unit of Calf intestinal alkaline phosphatase (CIP) per μg of protein (Quick CIP, NEB) or with CIP + EDTA (50mM) to inhibits its activity per μg of protein at 37° for 1 h; before performing the regular IP protocol.

Cell fractionation

To collect proteins enriched in different cellular compartments, cell pellets were resuspended in different buffers to separate cytoplasm, nuclear, and chromatin fractions. Extraction of the cytoplasmic fraction was performed by incubation for 2 min on ice in lysis buffer A (20 mM Tris pH 7.4, 10% glycerol, 10 mM KCl, 0.2% NP-40, 1 mM EDTA, 0.6 mM β-mercaptoethanol) supplemented with 1X protease inhibitor cocktail and 1 mM PMSF. Following centrifugation at 11,300 x *g*, 4°C, the supernatant containing the cytoplasmic fraction was collected and the pellets were re-suspended in nuclear extract buffer B (20 mM Tris (pH 7.4), 20% glycerol, 10 mM KCl, 0.4 M NaCl, 1 mM EDTA, 0.6 mM β-mercaptoethanol) supplemented with 1 mM PMSF and 1X protease inhibitor cocktail. Resuspended cells were incubated for 30 min on ice and centrifuged at 11,300 x *g*, 4°C and following centrifugation the supernatant containing the nuclear fraction was collected and the pellets were re-suspended in acid extraction buffer (aqueous 2 M HCl, 50% Glycerol, 250 mM β-Mercaptoethanol) for 3 min and centrifuged at 11,300 x *g*, both at room temperature. Following centrifugation, the supernatant containing the chromatin fraction was collected and neutralization buffer (1 M Tris pH 7.4, 1 M NaOH) supplemented with 1X protease inhibitor cocktail was added to each extract.

Immunofluorescence

For SART1 subcellular localization analysis, *SART1*-proficient and -deficient (silenced) HeLa cells were seeded in 4-well plates (5×10^4 per well) and were mock-treated or treated with 4 Gy of ionizing radiation (IR) to induce DNA damage 24 h after plating. Four hours after IR treatment, cells were washed once with PBS and fixed with paraformaldehyde (4%) for 15 min at room temperature, then washed again with PBS and stored at 4°C for 24 h.

For RIF1 and RAD51 recruitment analysis, HeLa cells were first seeded in 6-well plates (3×10^4 cells per well) and transfected with a siRNA targeting *SART1* or with a non-targeting siRNA as control using the Lipofectamine RNAiMAX Reagent (Thermo Fisher Scientific) following the manufacturer's instruction. One day after transfection, cells were trypsinized and reseeded in 24-well plates (5×10^4 cells per well) containing glass coverslips. In the next day, cells were treated with bleomycin (20 μg/mL) for 3 h. After treatment, cells were washed once with PBS and fixed with paraformaldehyde (4%) for 15 min at room temperature, then washed again with PBS and stored at 4°C for 24 h.

For both analyses, cells were then treated with permeabilization buffer (PBS/Triton X-0.1%) for 3 min and washed with PBS for 5 min, afterward cells were treated with blocking solution (PBS/BSA 3%) for 30 min. After blocking, primary antibodies were added to each well for 3 h

and then fluorescent AlexaFluor secondary antibodies were added for 1 h. Primary antibodies used were rabbit anti-SART1 (NBP1-89024, Novus Biological), Rabbit anti-RIF1 (PA5-57857, Thermo Fisher) Rabbit anti-RAD51 (PC-130, Calbiochem). All antibodies were diluted in PBS/BSA (1%). Finally, glass coverslips were positioned on glass slides with a drop of ProLong Gold antifade reagent with DAPI per coverslip on it and analyzed using a confocal microscope. To identify cells in S/G2 phase of the cell cycle, we used a mouse anti-Cyclin-B1 antibody (554176, BD-Pharmingen).

Fragment cloning and expression

To facilitate biochemical analysis, we generated three fragments of SART1. SART1 protein sequences from *Homo sapiens*, *Mus musculus*, *Rattus norvegicus*, *Danio rerio*, and *Xenopus laevis* were retrieved from UniProt. ClustalW algorithm was used to obtain a multiple alignment and identify the most highly conserved regions to guide the choice of functional SART1 regions. Based on the alignment result, a search for common PAR reader motifs (RGG/RG), prediction of disordered regions, and a literature search for known PARylated Serine residues, we divided SART1 proteins in three regions: fragment 1 (aa 1–250) containing the first putative PAR reader motif (R^{59}GGERGSGRRG^{69}) sequence and a coiled-coil motif (aa 157–231), fragment 2 (aa 235–490) containing a second putative PAR reader motif (R^{440}LRGRGRRR^{446}) sequence, and fragment 3 (aa 480–800) containing a cluster of known PARylatable Serine residues and a second coiled-coil motif (aa490-533).[8,12,38,68] Prediction of intrinsically disordered regions in SART1 was performed using PrDOS (https://prdos.hgc.jp/).

Each cDNA coding for fragments 1–3 was obtained by PCR using primers listed in Figure S7 and pFRT-HA-SART1 (38087, Addgene) as template. After purification, they were cloned in frame with a C-terminal FLAG tag into the multiple cloning site of pCMV6-entry using HindIII (NEB) and XhoI (NEB). Plasmids were Sanger sequenced to verify correct frame insertion and absence of mutations. Western blots using an anti-FLAG antibody were performed after transfection to confirm fragment size, expression, and stability.

Site-directed mutagenesis

Site-directed mutagenesis was performed to mutate R^{59}GGERGSGRRG^{69} sequence identified on the first part of SART1 sequence into A^{59}AAERGSGRRG^{69} using the QuikChange II Site-Directed Mutagenesis Kit (Agilent) following manufacturer's instructions and primers listed in Figure S7.

Clonogenic assay

UWB1.289 and UWB1.289+BRCA1 cell lines were used for clonogenic assays to assess sensitivity to DNA damage by ionizing irradiation and to three PARP inhibitors (olaparib (TMO-T3015, TargetMOL), rucaparib (TMO-T4463, TargetMOL) and talazoparib (TMO-T6253, TargetMOL) in *SART1*-proficient or -deficient (silenced) cells. For clonogenic assays performed to assess PARPi sensitivity in the UWB+B cell line, 4500 cells were seeded in each well in a 6-well plate; while for UWB, 6000 cells have been seeded in each well in a 6-well plate. The next day after plating, medium was changed with fresh medium containing a range of drug concentrations or fresh medium with vehicle (DMSO) as control. For olaparib and rucaparib the concentrations used were: 0.016, 0.08, 0.4, 2 and 10 μM; for talazoparib, the concentrations used were: 0.16, 0.8, 4, 20 and 100 nM.

For clonogenic assays performed to assess Ionizing Radiation (IR) sensitivity for UWB+B 8,000 cells were seeded in 60 mm plates, while for UWB 12,000 cells were seeded in 60 mm plates. The next day after plating, each plate was mock-exposed, or exposed to a range of IR doses: 0.25, 0.5, 1, 2, and 4 Gy.

For the analysis of combination (PARPi and IR) treatment, we followed the protocol for PARPi sensitivity testing with the following modification. Before adding media with vehicle (DMSO) or different drug concentrations, cells were exposed to IR (1 Gy). To avoid confounding due to the reduced viability caused by the IR treatment alone, results from cells treated with PARPi and IR were normalized using the sample treated with IR only.

In all cases, 7–10 days after treatment cells were fixed with methanol for 10 min at room temperature, stained with crystal violet 1X in PBS for 30 min at room temperature and washed with water. The day after, crystal violet has been extracted with methanol, transferred to 96 wells and absorbance measured at 540 nm.

QUANTIFICATION AND STATISTICAL ANALYSIS

Data are expressed as mean ± standard error of the mean (SEM) unless otherwise stated. Areas under the curves (AUCs) were calculated and statistical tests were performed using the Student's t test using Graph-pad Prism 8 and assuming normal distribution of the data. *p* values were determined by an unpaired two-tailed t-test. Intersections between different datasets were visualized using an Upset graph.[69]